The Dissertation Committee for Priyaveena Puvanakrishnan
certifies that this is the approved version of the following dissertation:

Near-infrared narrowband imaging of tumors using gold nanoparticles

Committee:

James W. Tunnell, Supervisor

Sunil Krishnan

Thomas E. Milner

Andrew K. Dunn

Konstantin V. Sokolov

Near-infrared narrowband imaging of tumors using gold nanoparticles

by

Priyaveena Puvanakrishnan, B.E., M.S.E.

Dissertation

Presented to the Faculty of the Graduate School of

The University of Texas at Austin

in Partial Fulfillment

of the Requirements

for the Degree of

Doctor of Philosophy

The University of Texas at Austin

December 2011

Dedicated to my husband, Narasimhan Rajaram

Acknowledgements

I am very fortunate to have worked under the guidance of my supervisor James Tunnell. His guidance, encouragement, and support through my years in graduate school have been invaluable. He has also made me a stronger person.

I would like to thank my committee members Konstantin Sokolov, Thomas Milner, Sunil Krishnan and Andrew Dunn for their valuable suggestions and comments. I would like to express my sincere gratitude to Dr. Sunil Krishnan for his help with animal studies and innumerable discussions on various topics. I would like to thank Nanospectra Biosciences Inc. for providing the gold nanoparticles. Especially, Dr. Jon Schwartz for helping and coordinating with *in vivo* studies.

I would like to thank Jaesook Park and Arnold Estrada for mentoring me and providing useful advice on research. I would like to thank my undergraduate research assistants; Ernest Puckett and Brandon Nichols for helping me put together the imaging system.

I am greatly indebted to my family. I thank them for all their love and support. My parents have been a great source of inspiration. I thank my sister and brother-in-law for their constant motivation. My husband is my pillar of strength and all my accomplishments would not have been possible without him. Thank you all!

Near-infrared narrowband imaging of tumors using gold nanoparticles

Priyaveena Puvanakrishnan, PhD
The University of Texas at Austin, 2011

Supervisor: James W. Tunnell

A significant challenge in the surgical resection of tumors is accurate identification of tumor margins. Current methods for margin detection are time-intensive and often result in incomplete tumor excision and recurrence of disease. The objective of this project was to develop a near-infrared narrowband imaging (NIR NBI) system to image tumor and its margins in real-time during surgery utilizing the contrast provided by gold nanoparticles (GNPs). NIR NBI images narrow wavelength bands to enhance contrast from plasmonic particles in a widefield, portable and non-contact device that is clinically compatible for real-time tumor margin demarcation. GNPs have recently gained significant traction as nanovectors for combined imaging and photothermal therapy of tumors. Delivered systemically, GNPs preferentially accumulate at the tumor site via the enhanced permeability and retention effect, and when irradiated with NIR light, produce sufficient heat to treat tumor tissue. The NIR NBI system consists of 1) two LED's: green (530 nm) and NIR (780 nm) LED for illuminating the blood vessels and GNP, respectively, 2) a

filter wheel for wavelength selection, and 3) a CCD to collect reflected light from the sample. The NIR NBI system acquires and processes images at a rate of at least 6 frames per second. We have developed custom control software with a graphical user interface that handles both image acquisition and processing/display in real-time. We used mice with a subcutaneous tumor xenograft model that received intravenous administration and topical administration of gold nanoshells and gold nanorods. We determined the GNP's distribution and accumulation pattern within tumors using NIR NBI.

Ex vivo NIR NBI of tumor xenografts accumulated with GNPs delivered systemically, demonstrated a highly heterogeneous distribution of GNP within the tumor with higher accumulation at the cortex. GNPs were observed in unique patterns surrounding the perivascular region. The GNPs clearly defined the tumor while surrounding normal tissue did not indicate the presence of particles. In addition, we present results from NBI of tumors that received topical delivery of conjugated GNPs. We determined that tumor labeling using topical delivery approach resulted in a more homogenous distribution of GNPs compared to the systemic delivery approach. Finally, we present results from the on-going *in vivo* tumor margin imaging studies using NIR NBI. Our results demonstrate the feasibility of NIR NBI in demarcating tumor margins during surgical resection and potentially guiding photo-thermal ablation of tumors.

Table of Contents

List of Tables

List of Figures

Chapter 1

Contrast agent-based imaging for surgical guidance

1.1 Motivation

The identification and removal of residual tumors remains a challenge during intraoperative surgeries. An important cause of recurrence of cancer at the site is due to either incomplete surgical removal of the tumor or the presence of small residuals that are invisible to the surgeon. Several studies have identified resection margin status as an important prognostic factor; a margin-positive resection strongly predicts early recurrence and poor survival rates.[1-7] For example, with pancreatic cancer, the challenging nature of resection along the retroperitoneal margin results in patients frequently undergoing incomplete resection.[1-3, 8, 9] The challenge lies in accurately identifying tumor margins and successfully performing margin-negative resection during

surgery.[10] Intraoperative identification of positive margins is also not routinely undertaken since the resection is usually carried out all the way to the retroperitoneal margin and additional tissue cannot be safely resected. Therefore, the identification of positive margin occurs only after the surgery when the pathology report is prepared.

In the case of breast tumors, upon initial diagnosis, surgical removal followed by adjunctive therapy is the primary standard of care.[11] The main purpose of breast conservation surgery is to remove the entire tumor and obtain clear margins (a zone devoid of tumor) around the cavity to decrease the chance of local tumor recurrence. However there are challenges identifying the residual tumor at the margin. Because of this, inadequate margins are found at the first operation in 20-55% of breast cancers removed by open lumpectomy.[12-14] In addition, 75-90% of recurrences occur at the site of the original lumpectomy.[15-17] It has been reported that the presence of clean surgical margins will reduce the 3-5 year rate of local recurrence. Accordingly, techniques that result in improved initial surgical margins may have a significant impact on treatment costs, on disease progression and possibly on survival.

Currently, for surgical removal of nonmelanoma skin cancers, the surgeon is required to take an excess margin of skin around the lesion to account for non-clinically relevant spread of the tumor. This excess margin can result in a larger scar and greater cosmetic and functional deformity. Non-melanoma skin cancers such as squamous cell carcinomas (SCCs) are typically removed using Mohs surgery. Mohs surgery involves

sequential removal of small layers of skin followed by examination under the microscope until the samples indicate no residual features or positive margins of SCC. Mohs surgery requires multiple excisions, with preparation of frozen sections and examination requiring 20 to 45 minutes per excision.[18] In the case of large SCCs, several excisions may be required, and the total visit time may extend to several hours. Noninvasive imaging techniques for intraoperatively revealing the tumor margins and limiting the size of these surgical excisions would potentially spare patients from requiring expensive grafting and reconstruction procedures. Therefore, an intraoperative device is needed to provide information to guide precise tumor resection.

1.2 Current imaging approaches

While traditional imaging techniques have been used to identify the presence or location of tumors, current investigations often focus on the use of enhancing contrast agents for these traditional techniques or on entirely new methods. Several imaging techniques are being investigated for use in the identification of tumor and its margins, including the use of systemically delivered agents to identify the tumor. Near-infrared absorbing nanocages, nanorods and nanoshells have been used in conjunction with optical coherence tomography and optoacoustic (photoacoustic) tomography to provide contrast.[19-23] Some techniques rely upon the endogenous optical properties of tissue or

molecularly targeted agents.[24] In general, these techniques focus on the identification of the cancer rather than precise delineation of its boundaries.

Various techniques have been investigated to identify the margins of tumors as an aid to surgery. Optical spectroscopy has been used to distinguish between normal brain tissues from tumor. In one example, infiltrating tumor margins were distinguished from normal brain tissue with a sensitivity of 94% and a specificity of 93%. This work relied on the optical properties of normal brain tissue compared to tumors, and the demonstrated level of sensitivity and sensitivity was lower than desired. [25-27]

Others have used conventional contrast agents for margin identification. In one example, a paramagnetic iron oxide conjugated with a Cy5.5 near-infrared emitting dye was delivered intravenously, allowed to accumulate in the tumor. Thereafter, the animals were sacrificed. Blood was drained from the animals to reduce background (potentially reducing the background caused by blood in the dye-emission wavelength) and the tumors were imaged. The border of the tumor as indicated by a probe correlated well with other measurements of the tumor boundary.[28] In other work, a near-infrared fluorescent small molecule specific for PSMA was used to provide image guidance for surgery.[29] Two challenges for this approach include the specificity and universality of the target (PSMA) and the background resulting from near-infrared fluorescence of blood/hemoglobin.

Quantum dots have also been investigated as a conventional contrast agent using the fluorescent emission properties of these particles.[30] More recently, a targeted bioconjugate of the CY5.5 near-infrared fluorescing dye to a chlorotoxin with an affinity for MMP-2 was used for fluorescent imaging. This group achieved positive results in animal models by detecting the fluorescent emissions from this conjugate.[31] Further study may be required to determine any potential cross-reactivity in humans and the photobleaching of the near-infrared dye in the operating room light. Additionally, fluorescent techniques may be hampered by the natural auto-fluorescence of human blood and tissue.

1.3 Narrowband imaging

Narrow band imaging (NBI) is a diagnostic technique clinically available today and used in several imaging applications to image morphology near the surface of tissue. Narrowband imaging is based on the phenomenon that the depth of light penetration in tissue depends on its wavelength, with longer wavelengths penetrating deeper into tissue. This technique illuminates tissue with a broadband source (e.g., white light) and uses narrowband filters in two or more wavelength bands in the visible spectra to capture reflected light. The different wavelength bands are differentially absorbed or reflected by different tissue components, in particular hemoglobin, and allow the visualization of the vasculature near the surface. Again, this technique commonly relies upon the optical properties of endogenous tissue to distinguish healthy and abnormal tissue. The common

wavelength bands utilized are in the blue and green area of the spectra, and some techniques also utilize a band in the red wavelength. Relying on the absorption of each of these bands by hemoglobin, and the different transmission depths of these wavelengths into tissue, allows the visualization of surface or sub-surface vasculature or morphology. In recent years several research groups have used Narrow Band Imaging combined with endoscopy to differentiate normal and cancerous tissue in the Barrett's esophagus, oral cavity.[32,33] However, traditional narrowband imaging relies on differences in the endogenous optical properties of tissue, and is thereby limited in applications and specificity for many disease indications. [34-37]

1.4 Metal nanoparticles for imaging and therapy

Metal nanoparticles have recently gained enormous interest as exogenous contrast agents in a variety of biomedical applications related to cancer detection and treatment. Metal nanoparticles include gold nanorods, gold nanoshells, carbon nanotubes, gold nanospheres, metal nanowires, semiconductor quantum dots and other nanoparticles produced from a variety of substances. As contrast agents, metal nanoparticles like gold nanoshells (GNSs) and gold nanorods (GNRs) have been used to detect and image individual cancer cells *in vitro* and in solid tumors *in vivo*. These gold nanoparticles (GNPs) can be designed to either absorb or scatter light in the visible and infrared regions of the electromagnetic spectrum.[38] In particular, their plasmon resonance can be tuned in

the near infrared region where there is minimal absorption of light by biological chromophores and optimal penetration of light through tissue. [39, 40, 41] The biologically inert surface of GNPs also enables bioconjugation with cancer targeting ligands, thus facilitating selective binding to *in vivo* targets.[42-44] In addition, gold nanoparticles possess strong photostability [45] and are thermally stable.[46] The high thermal conductivity of gold makes them efficient for transferring heat to the surrounding. These unique optical, chemical and physical properties make them ideal candidates for molecular and cellular imaging, enhancing cancer detection and treatment.

1.4.1 Gold nanoparticles as therapeutic agents

Gold nanoparticles can absorb large amounts of energy due to their large optical absorption cross sections, when irradiated with a near-infrared (NIR) light and can effectively convert them to heat. In addition, GNPs injected systemically through the tail vein, passively extravasate from leaky tumor vasculatures and preferentially accumulate in tumors due to the enhanced permeability and retention (EPR) effect.[47,11] This tumor specific accumulation and NIR activation can be exploited for thermal ablation of solid tumors using NIR illumination. Several *in vitro* studies have used NIR absorbing GNSs [42, 48] and GNRs [49-54] for photothermal ablation of cells and tumors. Recently, *in vivo* models for photothermal ablation of tumors using GNSs and GNRs have been demonstrated by West *et al.* [11, 55] , El-Sayed *et al.*[56] and Goodrich *et al*.. [57]

1.4.2 Gold nanoparticles as contrast agents for imaging

Because of optical tunability and high absorption and scattering cross sections, GNPs have been used as *in vitro* and *in vivo* contrast agents in several imaging applications. In addition to their potential applications as therapeutic agents, gold nanoparticles have gained popularity as scattering-based contrast agents in *in vitro*[58,59] and *in vivo* [60] imaging strategies combined with therapy. Loo *et al* successfully bioconjugated GNSs with HER2 antibodies to target human mammary adenocarcinoma cells *in vitro*.[9] Targeted gold nanoshell bioconjugates demonstrated increased optical contrast for imaging human breast cancer cells using *in vitro* dark field microscopy.[44] In addition, GNSs with high scattering cross sections have been used as effective contrast enhancement agents *in vitro* using optical coherence tomography.[61] Wang *et al.* demonstrated enhanced contrast between blood vessels and the surrounding brain tissue due to gold nanoshell absorption using *in vivo* photoacoustic tomography (PAT).[62] El-Sayed *et al.* have used anti-EGFR gold nanorods to detect and image two oral sqaumous carcinoma cell lines, HSC 313 and HOC 3.[63, 64] The GNRs were found to specifically and homogenously bind to the surface of cancer cells with 600% greater affinity than non-malignant cells. Recently, researchers have taken advantage of the two-photon luminescence properties of GNPs. Some studies have used GNSs to image the 3D distribution in tumors [46] and image live breast cancer cells with immunotargeted GNSs using *in vitro* two-photon microscopy. [65]

1.5 Narrow band imaging using gold nanoparticles

Most imaging techniques utilize GNPs as contrast agents for enhanced visualization of targeted cancer cells at the microscopic level or as absorption agents to enhance contrast between blood vessels and surrounding tissue. However, in studies involving identification of tumor margins (e.g. breast tumor margin detection), one would require a wide-field, non-contact method to image and resect the positive margins and ablate in situations where resection is impossible. We use GNPs' strong NIR absorption to demonstrate enhanced contrast between GNPs accumulated in the tumor and the surrounding vasculature and tissue using narrowband imaging.

The primary objective of this research is to develop real-time, wide-field, non-contact method to image the tumor and its margins using gold nanoparticles as contrast agents during surgery and perform photo thermal ablation of the residual tumor if necessary. Chapter 2 describes the design and development of a prototype NBI system. We validate the performance of the bench top NBI system on tissue-simulating phantoms and demonstrate the system's capability to image tumors using gold nanoshells as contrast agents. Chapter 3 presents the optimized, clinical grade imaging system that can perform real-time imaging of samples at approximately 6 frames per second. We have demonstrated its real-time imaging capability using tissue-simulating phantoms. The optimized system is portable and noncontact, facilitating clinical compatibility particularly in a sterile operating field. In chapters 4 and 5, we perform studies using

tumor xenografts to determine the ideal parameters for tumor targeting such as nanoparticle type (gold nanoshells or gold nanorods), dosing strategy (single or multiple) and delivery method (systemic or topical). In chapter 6, we evaluate the feasibility of *in vivo* real-time imaging of breast and pancreatic tumors and tumor margins. We establish an animal model with minimal residual disease to mimic positive resection margins of pancreatic cancer. Finally, we demonstrate the feasibility of combined imaging and image-guided therapy of pancreatic cancers.

Chapter 2

Near-infrared narrowband imaging

2.1 Introduction

In recent years several research groups have used NBI combined with endoscopy to differentiate normal and cancerous tissue in the oral cavity,[32] esophagus[33] and colon.[66] The technique involves illuminating light in narrow wavelength bands to enhance contrast of important endogenous tissue chromophores such as hemoglobin in blood vessels. By shining narrow bands of light of lower wavelengths, one can differentiate vascular patterns and the surrounding tissue surfaces with greater visual contrast. Visualization of increased vasculature (i.e. angiogenesis) is an important indicator of certain early cancer. Previous studies reported with NBI have used endogenous chromophores to distinguish normal from cancerous tissue.

Here we report a new application of NIR NBI for imaging tumors using exogenous contrast agents. In particular, we report the use of GNSs, one of the class of near-infrared-absorbing materials available, as the exogenous contrast agent. We used broadband light for illuminating the target and imaged select wavelength bands in the visible (VIS) and NIR regions to enhance visualization of hemoglobin and GNSs, respectively. We combined the absorption properties of hemoglobin and GNSs in the respective VIS and NIR wavelengths to specifically identify the tumor regions. We quantitatively determined the narrow wavelength bands providing high contrast for hemoglobin and GNSs using tissue simulating phantoms and found the optimum NBI wavelengths in the VIS and NIR to be 540 - 580 nm and 620 - 900 nm, respectively. We then performed *ex vivo* NBI of murine tumors accumulated with GNSs using two bands: 580 nm for highlighting blood and 810 nm for highlighting GNSs.

2.2 Materials and Methods

2.2.1 NBI system

We designed and developed a prototype NIR NBI system to image tumors and surrounding normal tissue in wide field. A schematic of the NBI system is shown in Figure 2.1. We used a quartz-tungsten-halogen lamp (100 W, Newport Stratford Inc., Stratford, CT) for white light illumination (400-1100 nm), a liquid crystal tunable filter (LCTF; Meadowlark Optics Inc., Frederick, CO) for wavelength selection and a cooled

12-bit CCD (CoolSnap, Photometrics, Tucson, AZ) to collect reflected light. We used a bifurcated fiber optic cable (Dolan Jenner, Boxborough, MA) to focus the light directly onto the sample. The LCTF is a tunable band pass filter that has a full width at half maximum (FWHM) of ~5 nm tuned to operate in a wavelength range of 400-1100 nm.

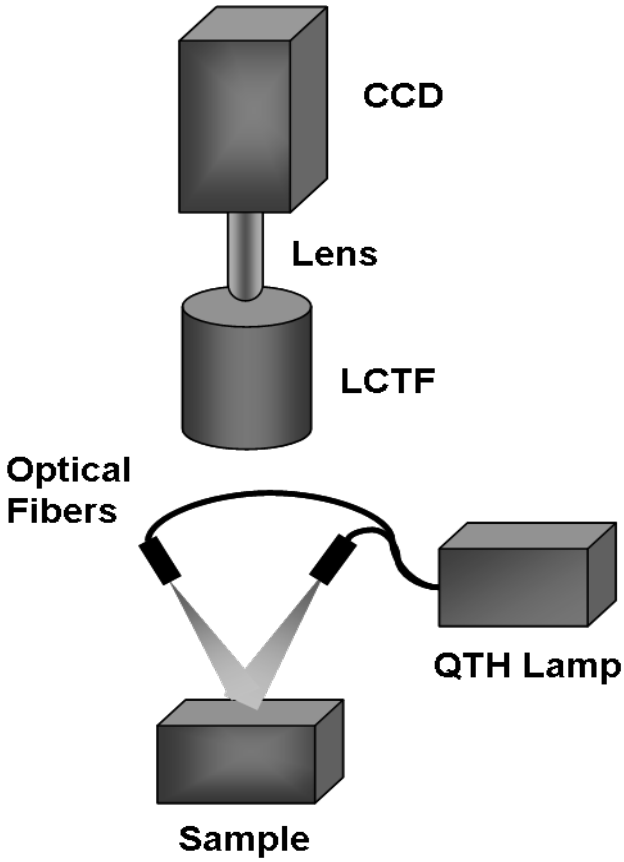

Figure 2.1: Schematic of NBI system

2.2.2 Gold/Silica Nanoshell Fabrication

Nanoshells were obtained from Nanospectra Biosciences, Inc. (Houston, TX). The GNSs fabrication is based on the method of Oldenburg[38]. Briefly, gold colloids, 1-3 nm in diameter, were grown over an aminated 120 ± 12 nm core of colloidal silica (Precision Colloids, LLC, Cartersville, GA). Gold colloid and the particles were then further reacted with $HAuCl_4$ in the presence of formaldehyde causing the gold surface to grow and coalesce, ultimately forming a complete shell. The gold surface was then pegylated using thiolated polyethylene glycol (SH-PEG) (Laysan Bio, Huntsville, AL) to improve stability and blood circulation. GNSs formation and dispersion in solution were assessed using a UV-Vis spectrophotometer. Figure 2.2 illustrates the extinction spectrum of the GNSs used in this study.

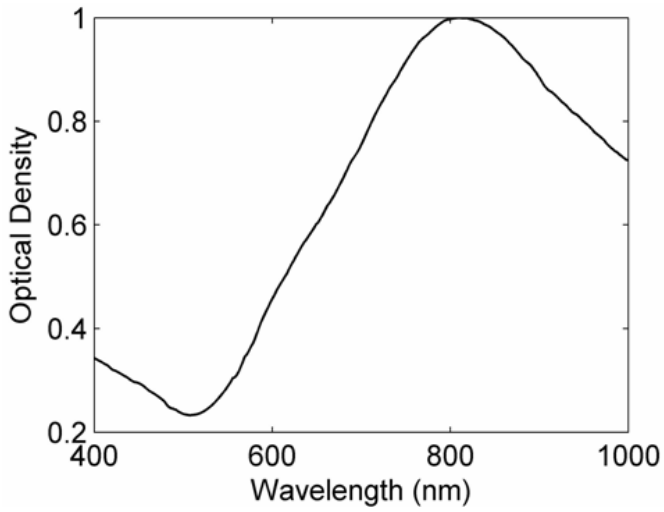

Figure 2.2: UV-VIS extinction spectrum of GNSs. A concentration of 2.66 x 10^9 (100x dilution factor) particles/ml produced a peak OD of ~1.

A concentration of 2.66 x 10^9 (100x dilution factor) particles/ml produced a peak OD of ~1. The particles were designed to have a core size of 120 nm and a shell thickness of 15 nm resulting in an extinction peak between 800 and 810 nm. Based on the Mie theory calculations for these GNSs, the absorption cross-section was approximately 25 % of the extinction cross-section (approximate scattering cross-section was 5.6 x 10^4 nm^2 and the absorption cross-section was 2 x 10^4 nm^2). For passive targeting, a thiolated polyethylene glycol (SH-PEG) (Laysan Bio, Huntsville, AL) was added to the shell surface by combining 5 μM SH-PEG and GNSs in deionized water for 12 hr, followed by diafiltration to remove the excess SH-PEG. The GNSs were in 1L volume, at a concentration of approximately 4 x 10^9 particles/mL. This corresponds to a particle concentration of ~7 pM when 5 μM PEG-SH is added. We used 10% trehalose to

suspend GNSs for injection because GNSs exhibit greater long-term stability in trehalose compared to PBS. In addition, 10% trehalose is iso-osmotic with blood.

2.2.3 Tissue Phantoms

To determine the optimum wavelength bands and the GNSs detection limit, we used tissue-simulating phantoms of known optical properties. These phantoms were fabricated using polystyrene microspheres (diameter = 1.025 μm; Polysciences, Warrington, PA) to simulate scattering and hemoglobin (Sigma, St. Louis, MO) and GNSs (Nanospectra Biosciences Inc, Houston, TX) to simulate absorption. We used Mie theory to calculate the reduced scattering coefficient ($\mu_s'(\lambda)$) and a spectrophotometer (DU 720, Beckman Coulter, Fullerton, CA) to measure the absorption spectra of hemoglobin and GNSs.

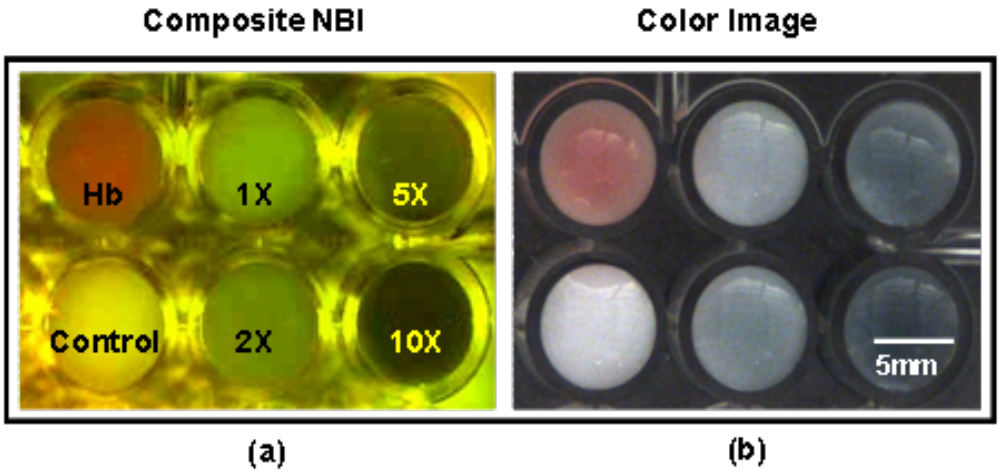

Figure 2.3: Matrix of tissue simulating phantoms. (a) Composite NBI image (b) Standard color image. 1X, 2X, 5X and 10X refer to varying GNSs concentrations where X is 1.14 x 10^9 particles/ml.

We prepared a set of six tissue simulating phantoms as shown in Figure 2.3. Phantom 1 (control phantom) contained polystyrene microspheres in de-ionized water and phantom 2 (hemoglobin phantom) contained polystyrene microspheres and hemoglobin ([Hb]=2 mg/ml; μ_a (λ=580 nm) = 0.36 mm^{-1}). Phantoms 3-6 contained varying concentrations of GNSs (1X, 2X, 5X and 10X, where X refers to 1.14 x 10^9 particles/ml) in polystyrene microsphere solutions. All phantoms contained the same density of polystyrene microspheres (μ_s'(λ_0 = 630 nm) = 1 mm^{-1}). The range of μ_a and μ_s' for phantoms 3-6 at the peak extinction wavelength of GNSs (810 nm) was 0.02 – 0.21 mm^{-1} and 0.82 – 1.38 mm^{-1}, respectively. The μ_s' of phantoms 3-6 represents scattering from both GNSs and polystyrene microspheres at 810 nm. GNSs concentration of 1X represents the physiological concentration shown to accumulate in tumors.[67,68] We fabricated and imaged one additional GNSs phantom with a concentration of 0.5X; however, this phantom demonstrated minimal contrast from the control phantom.

2.2.4 Animal Model

We demonstrated NBI in tumor xenograft animal models of colorectal cancer. We used four to five week old Swiss *nu/nu* mice weighing 25-30 g each at four to five weeks old. Each animal was inoculated subcutaneously with human colorectal cancer cells (HCT116, ATCC #CCL-247). The test group (n = 5) received 4.7 µl/g of GNSs solution standardized to an optical density of 97 at 811 nm (2.66 x 10^{11} particles/ml) injected

intravenously via the tail vein. The control mouse received 4.6 μl/g of the trehalose vehicle. Previous studies show that the maximum accumulation of GNSs in tumors is 24 hours post injection.[67] Therefore, we sacrificed the mice after 24 hr following GNSs injection and excised the bulk tissue containing the tumor from the mice to expose the subcutaneous side of the tumor for imaging. We performed imaging within 10-15 minutes of tumor excision. Excess blood from the tumor extraction was minimal and did not obscure the field of view.

2.3 Results

2.3.1 Optimum imaging wavelengths

We determined the optimum imaging wavelengths for NBI using tissue-simulating phantoms. Optimum imaging wavelengths are the wavelengths providing maximum contrast between hemoglobin and GNSs in the tumor. We collected hyperspectral images of the set of tissue-simulating phantoms from the visible to NIR regions (500 – 900 nm) to determine the optimum imaging wavelengths. We constructed an image cube by collecting intensity images of the phantoms at 22 different wavelengths by tuning the LCTF.

In our study, the contrast was evaluated quantitatively and defined as the luminance ratio (ratio of the difference between sample intensity and background intensity to background intensity) according to Weber's law.[69] In the contrast calculation,

the background intensity is that of the control phantom and the sample intensity corresponds to hemoglobin and GNSs phantoms. We selected a small region of interest (100 x 100 pixels) from the imaged sample for each wavelength to calculate contrast for the hemoglobin phantom and one GNSs phantom (10X).

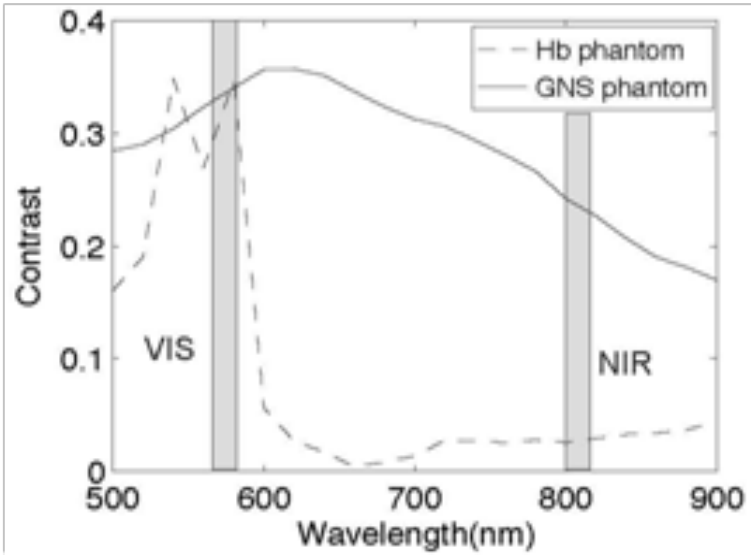

Figure 2.4: Contrast of hemoglobin phantom and GNS phantom in VIS-NIR region. The shaded areas represent the NBI wavelengths bands. (VIS image at 580 nm and NIR image at 810 nm)

A contrast plot for hemoglobin phantom and the GNS phantom in the wavelengths ranging from 500 – 900 nm is shown in Figure 2.4. The hemoglobin phantom contrast peaks at 540 nm and 580 nm, corresponding to the Q-bands of oxy-hemoglobin. The hemoglobin phantom contrast is minimal beyond 620 nm. The GNS phantom's contrast remains high throughout, with the peak at approximately 620 nm. The

contrast peak of the GNS phantom appears to have a blue shift relative to the ~800 nm peak observed in the extinction spectrum of Figure 2.2. Therefore, the optimum wavelength bands for enhancing contrast of hemoglobin and GNSs are 540- 580 nm and 620 – 900 nm, respectively. The subsequent NBI images use two bands: 1) VIS image: 580 nm for highlighting blood and 2) NIR image: 810 nm for highlighting GNSs. The shaded areas seen in Figure 2.4 represent the NBI wavelengths bands.

2.3.2 NBI of tissue phantoms

We collected narrow band images of tissue simulating phantoms to demonstrate the concept of NBI using the wavelength bands identified in the previous section. Using the standard RGB format, we assigned the red channel to the VIS image and the green channel to the NIR image. The composite NBI image was constructed by overlaying the two images as shown in Figure 2.5a. The composite narrow band image visually provides enhanced contrast of the hemoglobin phantom and the GNS phantom as compared to the standard color image shown in Figure 2.5b. To further demonstrate the NBI image characteristics, we selected small areas from the tissue phantom matrix of VIS and NIR grayscale images and the composite NBI image to present the NBI concept (Figure 2.5).

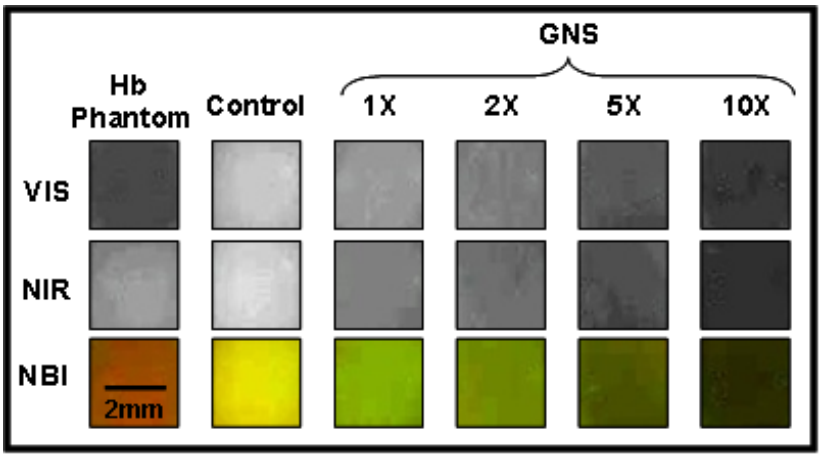

Figure 2.5: NBI images of small areas from tissue phantom matrix to demonstrate NBI image characteristics.

We observe high visual contrast of the hemoglobin phantom in the VIS grayscale image resulting in a bright red NBI composite image for the hemoglobin phantom. The control phantom has relatively little contrast in either VIS or NIR band resulting in a bright yellow composite NBI image. The GNS phantoms exhibit increasing contrast with higher GNS concentration resulting in an increasingly green NBI image as GNS concentration increased. These tissue phantoms provide an estimate of the detectable concentration of GNS within tissue.

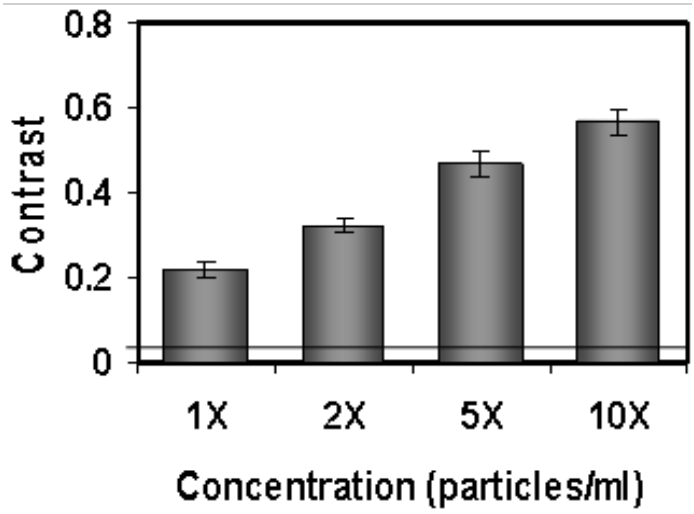

Figure 2.6: Contrast provided by GNS phantoms to estimate detectable concentration in tissue. The error bars represent the ratio of standard deviation to mean signal intensity for different GNS concentrations. The black line represents the background noise.

The physiological concentration of GNSs in tumor (1X) provides at least 20 % contrast from the background noise (3 %) indicated by the line in Figure 2.6. The background noise is the ratio of standard deviation to mean signal intensity of the control phantom. However, we observe that the concentration of GNSs providing more than 40 % contrast is between 5X and 10X.

2.3.3 NBI of murine tumors

We performed *ex-vivo* imaging of Swiss *nu/nu* mice inoculated with human colon cancer cells. Narrow band images of both the control mouse and GNSs injected mice were collected. A small portion from the tumor was selected to illustrate the micro-distribution

of hemoglobin and GNSs using the NBI technique. In the *ex-vivo* NBI images, the blood vessels are clearly visible in the VIS image as seen in Figures 2.7a and d.

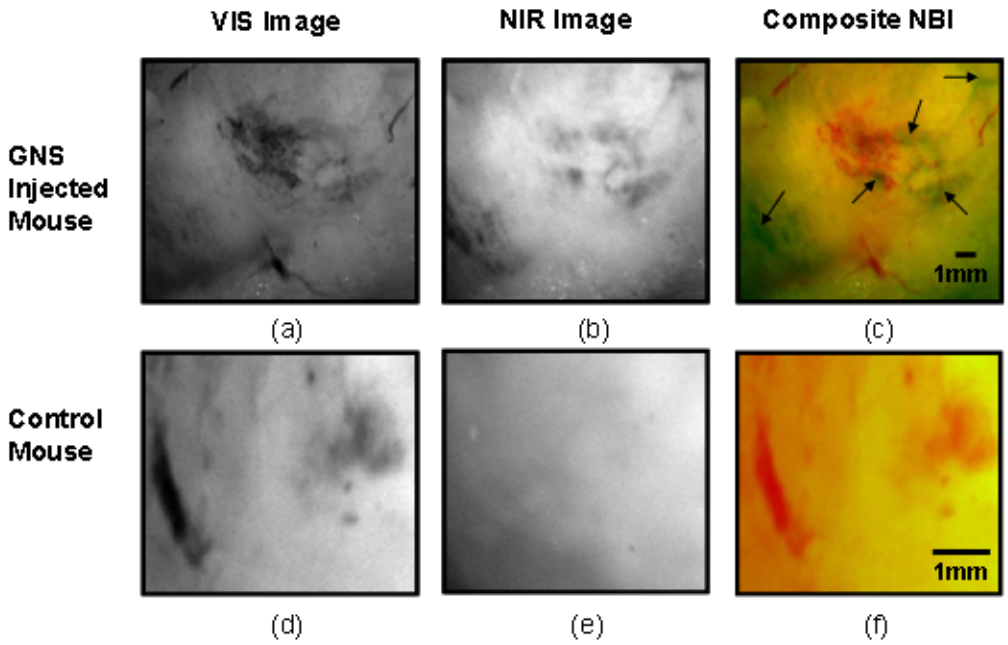

Figure 2.7: Upper panel: Narrow band images of human colon tumor. (a) Grayscale VIS image (580 nm) (b) Grayscale NIR image (810 nm) (c) Composite NBI image. The black arrows indicate GNSs in tumor. Lower panel: Narrow band images of control tumor (injected with trehalose). (a) Grayscale VIS image (580 nm) (b) Grayscale NIR image (810 nm) (c) Composite NBI image.

In the NIR image of the GNSs injected mouse, the GNSs accumulated tumor regions are clearly visible as dark areas as seen in Figure 2.7b. The control tumor indicates only the blood vessels as seen in Figure 2.7d. The advantage of NBI is clearly demonstrated in the composite NBI images. The composite NBI images of three other tumors accumulated with GNSs are shown in Figure 2.8 demonstrating the various

accumulation patterns seen among the tumors. The fifth mouse did not show significant particle accumulation by NBI. The black arrows in the images indicate focal regions of higher concentrations of the GNSs.

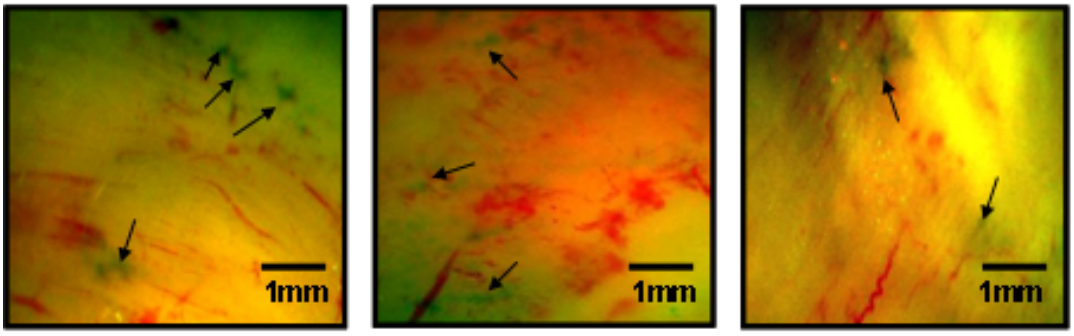

Figure 2.8: Composite NBI images of human colon tumors illustrating heterogeneous distribution of GNSs. The black arrows indicate GNSs in tumor.

2.4 Discussion

We have demonstrated NIR NBI for imaging GNSs systemically delivered to tumors. NBI uses a narrow band of wavelengths matched to the chromophores of interest to highlight contrast between tissue constituents and exogenous contrast agents. Although we have used GNSs as the NIR absorbing particle to provide contrast between hemoglobin and GNSs in tumor, one could use other nanoparticles such as nanorods[63] that can be tuned to absorb in the NIR or organic dyes such as Indocyanine Green.[70] In tissue phantoms containing only hemoglobin, we observe peak contrast between 540 and 580 nm (Figure 3) consistent with the absorption peaks of hemoglobin. In tissue

phantoms containing GNSs and no hemoglobin, we observe high contrast throughout the 500-900 nm range with a peak at approximately 620 nm. The GNSs with a core diameter of 120 nm and a shell thickness of 15 nm are anticipated to have an absorption peak around 800 nm[58]. While the peak contrast in tissue phantoms is blue shifted from that of pure GNSs in solution, the contrast remains high above 600 nm. Therefore, in order to avoid hemoglobin absorption contrast and maintain high contrast from GNSs, one should choose a band greater than ~620 nm. Based on this analysis, hemoglobin and GNSs contrast can be enhanced by selecting bands between 540 – 580 nm and 620 – 850 nm, respectively. In addition, as we move from the visible to NIR wavelengths, the scattering from tissue decreases, allowing for imaging of GNSs at greater depths. Therefore, we chose to image tissue phantoms and murine tumors in two bands: VIS image (580 nm) and NIR image (810 nm).

The tissue phantom images obtained using the optimum imaging wavelengths demonstrate the concept of NBI (Figure 2.3a). Figure 2.5 depicts the intensity variations due to varying concentrations of GNSs. In the composite NBI image, we observe the yellow color (control) to correspond to the tissue background. The hemoglobin phantom is assigned a red channel to depict the color of blood in tissue. We observe that as the concentration of GNSs increase, the yellow intensity decreases due to increase in absorption, which is shown by the increasing intensity of green color.

Figures 2.7 and 2.8 demonstrate magnified *ex-vivo* images of mice inoculated with human colon cancer cells and injected with GNSs. Although we did not quantify the imaging depth, the imaging depth should be related to tissue optical properties. Based on the mean free path (mfp), the imaging depth in the NIR is approximately 1 mm (the estimated mfp for rat skin is ~760 μm at 810 nm) [71]. We observe GNSs labeled in green are clearly distinguishable from blood vessels labeled in red. The black arrows highlight regions indicating the presence of GNSs. The effects of uneven illumination resulted in the greenish background present in some of the composite NBI tumor images (eg. Figure 2.7c). In these images, the background should ideally be uniformly yellow in color. The punctate areas in these composite NBI images are GNSs. Improvement in the target illumination will eliminate shadows and hot spots in the collected images.

Although we assume that the average concentration of GNSs accumulated in the tumor is 1X, GNSs tend to accumulate in small focal volumes of high concentrations in tumors as seen in Figures 2.7c and 2.8. The contrast seen in these images can be related to the tissue simulating phantoms in Figure 2.5, suggesting the focal areas of high GNSs contrast have concentrations much higher than 1X. In addition, the heterogeneous distribution of GNSs suggests that the previously measured average 1X concentration for the whole tumor is actually located in focal regions. Although our images only show superficial tissue layers, recent studies suggest that GNSs accumulate in the tumor cortex,[72] and therefore, this focal heterogeneous distribution is volumetric, suggesting these "hot spots" may have concentrations many times the volumetric average values

previously reported. Using NBI, we observed GNSs accumulation in four out of the five mice injected with GNSs represented in Figures 2.7c and 2.8. We believe that the tumor identified with no accumulated GNSs possibly had very minimal particles accumulated at the tumor site due to problems with particle delivery. This may be due to inadequate delivery of GNSs to the tail vein during injection.

We observed a heterogeneous accumulation of GNSs in the GNSs injected mice. Previous studies have demonstrated this heterogeneous nature of GNSs distribution in tumor. Li *et al.* imaged the passive accumulation of GNSs in murine colon tumors grown in BALB/c mice using photoacoustic microscopy and found GNSs to accumulate heterogeneously in the tumor, characterized by high concentrations in the tumor cortex and very low concentrations in the tumor core.[72] Park *et al.* also reported heterogeneous nature of GNSs accumulation in tumor and found that GNSs were located in close proximity to blood vessels using two-photon luminescence technique.[46] *In-vivo* thermal therapy of GNSs accumulated tumor performed by Hirsch *et al.* have reported that the temperature distribution from NIR irradiation is non-uniform due to the diffuse distribution of GNSs over the tumor.[55] Recently, Diagaradjane *et al.* reported high concentrations of GNSs within the perivascular region of tumors accounting for the high temperature increase in this region that resulted in vascular disruption after radiation therapy.[73] Further macroscopic NBI imaging could be performed to better understand the cause of the varying pattern of GNSs accumulation and GNSs accumulation specificity within the tumor.

The composite narrow band images demonstrate the potential use of NIR NBI technique for identifying GNSs accumulations within tissue and suggest several applications to this technique. Given that these particles preferentially accumulate at the tumor site, one may potentially use NIR NBI clinically to identify tumors and their margins during surgery pre- and post-resection. Given the high photothermal efficiency of GNSs, NBI may be used as a combined imaging and photothermal therapy platform for both identifying and ablating tumors, their margins, and residual disease after resection. The narrow band images could potentially guide in precise photothermal therapy without causing damage to surrounding normal tissue. For basic science applications, the narrow band images of tumor accumulated with GNSs will aid in understanding the nature of particle distribution within the tumor. For example, as metal nanoparticles are actively being studied for photothermal treatment of solid tumors, one may wish to use NBI to image particle distributions within tumors of a test model (e.g. mouse tumor xenograft). As new applications for the use of NIR absorbing nanoparticles are developed, NBI can serve as a tool for distinguishing particle locations within tissue.

The proposed optical imaging technique is minimally invasive. The NBI system has simple instrumentation, is easily portable and is “non-contact” which facilitates clinical compatibility particularly in a sterile operating field. While we have demonstrated snapshot imaging in the current study, the simplicity of NBI instrumentation would allow for video rate imaging. The composite NBI image obtained containing the enhanced visualization of blood vessels and GNSs will help in

understanding the extent of angiogenesis at a macroscopic level. The feasibility of NBI could potentially be extended to imaging other types of tumors and vascular lesions as well.

Chapter 3

Optimized near-infrared narrow-band imaging system

3.1 Introduction

In Chapter 2, we presented a bench-top prototype of the NBI system. We demonstrated the feasibility of the technique on tissue-simulating phantoms and a colon cancer cell line. The instrument acquired snapshot images of the tumor and worked well for measurements on *ex vivo* tissue samples in the lab. However, clinical translation for the purpose of surgical guidance requires a nearly continuous feed or video-rate imaging of the tumor. Clinical translation also dictates an easily portable and compact system that can be easily moved between rooms. In this chapter, we discuss our efforts towards optimizing the size of the system as well acquiring real-time images of tissue-simulating phantoms.

3.2 Methods and Results

3.2.1 Second-generation NBI system - hardware

The prototype NIR NBI system described in Chapter 2 used a liquid crystal tunable filter (LCTF) for selecting wavelength bands. Although this is an efficient method of tuning wavelengths compared to individual filters, we deemed it unnecessary from both a technical as well economic standpoint. The LCTF can select wavelengths in 5 nm increments from 400-1100 nm and has a switching speed of approximately 100 ms. In addition, it is bulky and quite expensive. Our phantom experiments showed that we only needed two wavelength bands – one in the visible wavelength band and one in the NIR. We also need to switch faster than 100 ms to be capable of video-rate imaging (~30 images/s). Therefore, we replaced the LCTF with a filter wheel for multiple wavelength selection. The filter wheel can hold up to 5 filters and with the addition of a stable AC motor is capable of switching between filters every 30 ms. We used two band pass filters (Semrock, Inc., Rochester, NY): 1) a VIS filter centered at 536 nm with a bandwidth of 40 nm and b) a NIR filter centered at 536 nm with a bandwidth of 41 nm to image the blood vessels and GNRs, respectively. We incorporated an AC motor (DigiKey Corp., MN) to control the filter wheel rotation. The collection of images was timed to a trigger from an optical interrupt (DigiKey Corp., MN) that triggers at the respective filter positions. We used an achromatic lens (Edmund Optics, Barrington, NJ) instead of the manual focusing lens. We replaced the Coolsnap Photometrics CCD with a smaller and

inexpensive 12-bit CCD (Basler Pilot, Graftek Imaging, Austin, TX) without compromising any significant camera features.

Another change that could significantly impact the acquisition time is the choice of light source. We replaced the tungsten halogen lamp with a light emitting diode (LED) illumination system. The illumination system consists of two LED's (Tholabs Inc., Newton, NJ): green (530 nm) and NIR (780 nm) for illuminating the blood vessels and nanoparticles, respectively. Condenser lenses on both the LED's collimate the incident light on the sample. There are separate driver circuits to control the light output from each LED. The integrated real-time NIR NBI system is shown in Figure 3.1.

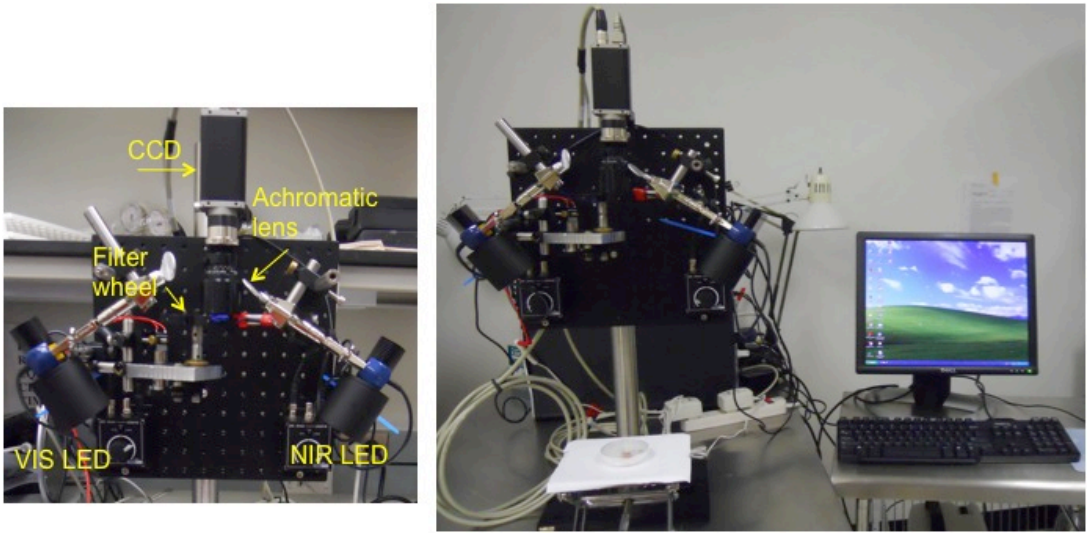

Figure 3.1: Integrated real-time NIR NBI system.

3.2.2 Second-generation NBI system - software

We developed custom control software in the LabVIEW® (National Instruments, Austin, TX) graphical programming environment to handle both image acquisition and processing/display. The image acquisition sequentially acquires sets of two images, one visible and one NIR at a camera exposure time of 10 ms. For real time imaging, the images are converted to 8 bit, binned by a factor of 4 resulting in an image size of 512 x 625 pixels. The custom control software constructs the composite narrowband image for display. This includes inverting and assigning the visible images to the red channel and NIR images to the green channel, respectively. Additionally, we developed a graphical user interface to display the images and provide controls to dynamically adjust the image features such as brightness and contrast of each channel. Figure 3.2 shows the GUI (front panel) that controls real-time acquisition and processing.

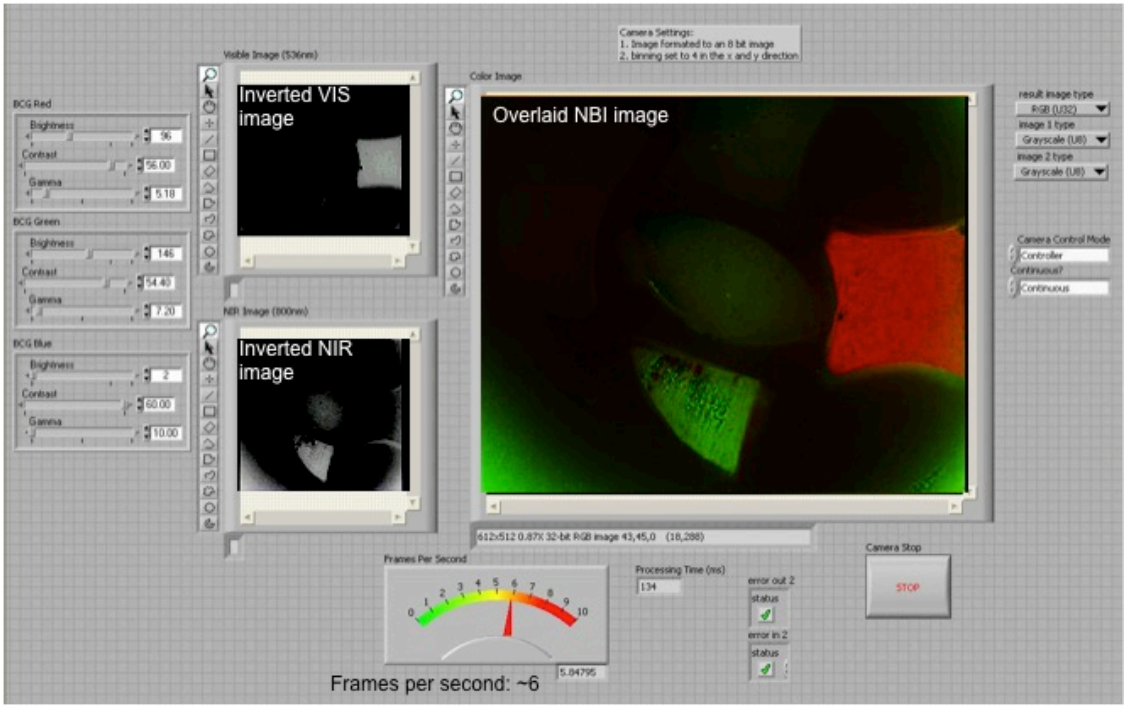

Figure 3.2: Snapshot of LABVIEW front panel that displays real-time image acquisition and processing at approximately 6 fps.

The second-generation system is capable of acquiring images at 6 frames per second. Although this is not quite video-rate yet, it is still a significant improvement over the first generation system.

3.2.3 Real-time imaging of tissue simulating phantom

We used a polydimethylsiloxane (PDMS) phantom to demonstrate the real-time image acquisition and processing capability of the NIR NBI system. The phantom consisted of red food dye to simulate absorption in the VIS wavelength and varying concentrations of

gold nanoshells to simulate absorption in the NIR wavelengths. The red square shaped phantom corresponds to the red food dye to simulate absorption in the VIS. The different shapes of the GNS phantoms correspond to different concentrations as indicated in Fig. 3.3. The figure shows excellent contrast between the different concentrations of GNSs. We also rotated the petri dish containing the phantoms and continuously acquired images. The image acquisition and processing was fast enough to keep up with the manual rotation and maintain the correct colors for the VIS and NIR phantoms.

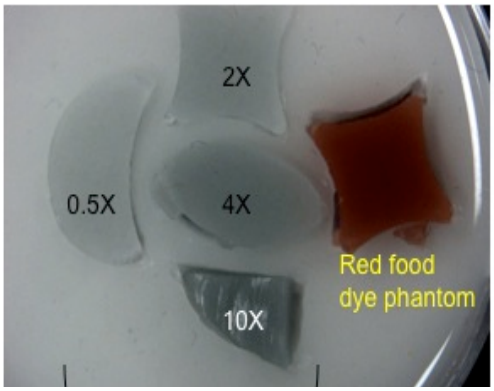

Figure 3.3: PDMS phantom used in the study. The red phantom contains a red food coloring dye that absorbs in the visible range. The other phantoms correspond to varying concentrations of GNSs. X corresponds to 1.10 x 10^9 GNSs/ml.

3.2.4 Determination of imaging and depth sensitivity:

We determined the depth sensitivity of the NIR NBI system using a 3D tissue-simulating phantom. We fabricated tissue-mimicking phantoms using TiO_2 mixed with PDMS (1.8 mg TiO_2/g PDMS) to simulate tissue scattering. After continuous stirring to ensure a

homogeneous mixture, the PDMS mixture was poured into a well containing openings in the walls at different depths. We inserted open capillary tubes (diameter = 400 μm) into the PDMS mixture through the openings to simulate blood vessels located at different depths. We injected gold nanorod concentrations ranging from ~ 8.5 x 10^{10} – 2.5 x 10^{13} particles/mL into these channels and acquired images using the NIR NBI system. Figures 3.4a and 3.4b shows the color and NIR NBI image of the phantom.

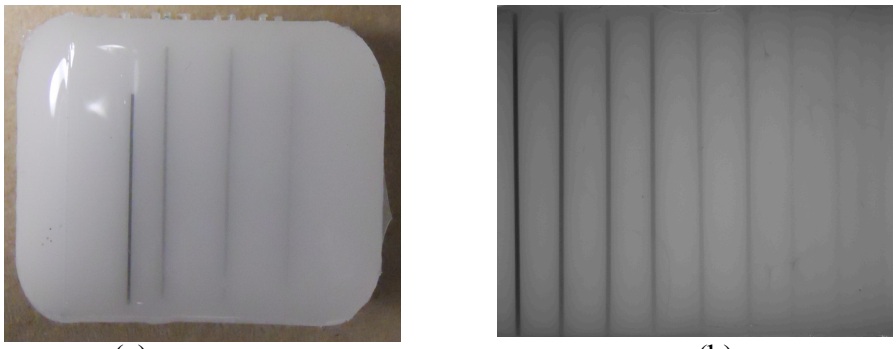

(a) (b)

Figure 3.4: (a) Color image of a phantom containing gold nanorods that are injected in various channels (b) Grayscale NIR NBI image of a phantom obtained at 769 nm. The channels were injected with gold nanorods of concentration 5.16 x 10^{12} particles/ml.

We calculated the contrast as a function of depth for the different GNR concentrations in the NIR wavelengths. The dilutions used in the study and their corresponding concentration values are shown in Table 3.1. The contrast was evaluated quantitatively and defined as the luminance ratio (i.e., the ratio of the difference between sample intensity and background intensity to the background intensity) according to

Weber's law. In the contrast calculation, the background intensity is from the TiO_2 substrate and the sample intensity corresponds to GNRs in each channel.

Table 3.1. Gold nanorod dilutions used in the study with the corresponding concentration values.

Dilution factors	**GNR concentration (particles/ml)**
Stock solution	2.58×10^{13}
15X	1.72×10^{12}
30X	8.6×10^{11}
80X	3.22×10^{11}
150X	1.72×10^{11}
300X	8.6×10^{10}

The experiment demonstrated a decrease in contrast values for higher depths as shown in Figure 3.5a. We observed that the contrast from different dilutions was minimal beyond 2 – 2.4 mm. The attenuation of the signal from the surface of the phantom to deeper channels was attributable to scattering from the substrate. Additionally, we observed the contrast from 150X dilution to be similar to the background noise suggesting that GNR concentrations below 1.72×10^{11} particles/mL in the channels were difficult to detect (Figure 3.5b) by the NIR NBI system and GNRs could not be differentiated from background noise at lower concentrations (300X).

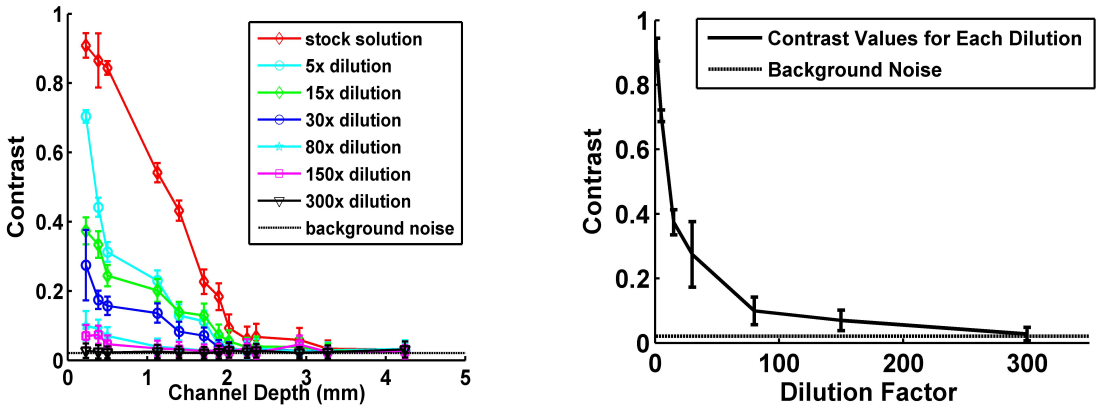

(a) (b)

Figure 3.5. (a) Contrast provided by GNRs at different depths for varying gold nanorod dilutions. (b) Contrast provided by GNRs on the top channel (approximately on the phantom surface) for different gold nanorod dilutions. The error bars represent the standard deviation of contrast values for each dilution. The black line represents the background noise (0.02).

3.3 Discussion

This chapter presents a second-generation instrument that is capable of real-time imaging in the clinic. The modified NIR NBI system used in this study provides benefits in terms of ease of operation and uniform illumination. Incorporating a powerful LED illumination system and a faster AC motor to control the filter wheel helped increase the acquisition rate to 6 fps. The NIR NBI was shown to provide excellent contrast up to a depth of at least 2 mm. As discussed in Chapter 2, the NIR NBI system could potentially provide a valuable method for surgical guidance during breast conserving surgery, pancreatic tumor resection and Mohs surgery for melanoma and non-melanoma skin cancers.

Chapter 4

Optimal parameters for efficient nanoparticle delivery

4.1 Motivation

The design as well as physical and chemical properties of nanoparticles is key to achieving effective tumor targeting and consequently improving cancer diagnosis and treatment. The results presented in Chapter 2 showed a heterogeneous accumulation of gold nanoshells in small focal regions. Given the long-term goal of using nanoparticles for ablative therapy, understanding particle accumulation and distribution profiles assumes significance for determining optimal therapeutic parameters. In this chapter, we discuss the studies performed to determine the effect of particle type, size and dosing strategy on tumor accumulation and biodistribution.

4.2 Introduction

In vivo tumor targeting using nanoparticles has primarily been achieved using EPR.[47] The tumors' inherent leaky vasculature and ineffective lymph system, enables systemically circulating nanoparticles to extravasate and accumulate in tumors due to the EPR effect.[57] Recent efforts have focused on active targeting, that exploits the over-expression of surface receptors on cancer cells by providing targeting ligands that can engage these receptors.[42-44] Choi *et al.* demonstrated that targeted nanoparticles could provide greater intracellular delivery of therapeutic agents to the cancer cells within solid tumors than their nontargeted analogs.[74] Although there is continuous effort to identify suitable targeting moieties and ideal design parameters for active and passive targeting, respectively, little is known about the effect of particle type and nanoparticle dosing strategies on tumor targeting and accumulation capacity.

Multiple dosing is most commonly used in chemotherapy, photodynamic and radiation therapy for improved cancer treatment efficacies.[75-77] Recently, a group demonstrated that a multiple dose of a photosensitizing agent MV6401 effectively induced tumor growth delay in mammary adenocarcinoma cells compared to a single dose.[78] In the present study, we investigate the effect of a multiple dosing strategy using pegylated gold nanoparticles to increase the *in vivo* tumor targeting competence.

As described previously in Chapter 1, pegylated GNPs are ideal for *in vivo* use as they are stable, non-toxic and possess unique optical and thermal properties that make

them effective contrast and photo-thermal agents.[53, 55] The poly ethylene glycol (PEG) coating on the gold nanopaticles' surface enables them to circulate longer and reduce non-specific uptake by the reticuloendothelial system (RES).[42] The RES, one of the body's filtration and defense mechanism, functions to remove foreign particles, irregular red and white blood cells as well as opsonized particles.[79] The liver and spleen that belong to the RES system are mainly responsible for the removal of different sized particles and hence these organs absorb a large percentage of systemically administered nanoparticles.[80] Most of the biodistribution studies have shown that approximately 50 - 60 % ID/g of nanoparticles are taken up by the liver and spleen, respectively.[81]

Particles of sizes ranging from 10 nm to 15 μm have different biodistribution and pharmacokinetic parameters.[82] Experiments from animal models suggest that sub -150 nm, neutral or slightly negatively charged entities can move through tumor tissue.[83] Recent data show that systemically delivered nanoparticles in the 50–100 nm size range that carry a very slight positive charge can penetrate throughout large tumors.[84] Therefore, nanoparticles in the 10 - 150 nm size range and with a neutral charge should have access to tumors when dosed into the circulatory system.[85] Perrault *et al.* have examined the particle size-dependent permeation of the tumor mass for 20 -100 nm size range, and revealed a difference in behavior for different sizes and demonstrated that particle design has tremendous consequences on tumor targeting behavior.[86]

In this chapter, we will investigate the effect of multiple dosing of GNPs and

nanoparticle type to improve tumor-targeting efficiency. We utilized large pegylated GNSs and small pegylated GNRs and compared the effect of size and shape of these particles on the tumor targeting efficiency. In addition, we compared the effect of single and multiple doses of GNRs and GNSs on *in vivo* tumor targeting. We will finally perform imaging of the tumors accumulated with both particle types for single and multiple dosing using the modifed NBI to evaluate the contrast enhancement in the images as a function of particle dosing.

4.3 Materials and Methods

4.3.1 Synthesis of pegylated gold nanoshells and nanorods

The nanoshells used in this study were fabricated as described in detail in Chapter 2. Nanorods were synthesized using the method developed by Jana *et al*.[87] Briefly, gold seed particles were prepared by adding 250 μL of 10 mM $HAuCl_4 \cdot 3H_2O$ to 7.5 mL of 100 mM CTAB with brief, gentle mixing. Freshly prepared 600 μL of ice-cold 10 mM $NaBH_4$ solution was added and the solution was mixed for 2 minutes. The nanorod growth solution was prepared by adding 40 mL of 100 mM CTAB, 1.7 mL of 10 mM $HAuCl_4 \cdot 3H_2O$, and 250 μL of 10 mM $AgNO_3$ followed by 270 μL of 100 mM ascorbic acid. To initiate nanorod growth, 840 μL of the seed solution was added to the growth solution, mixed gently, and left still for 40 minutes. Excess reactants were removed by centrifugation and re-suspension in de-ionized (DI) water. For *in vivo* applications, the

GNRs were PEGylated by the addition of 1 mM thiol-terminated methoxypolyethylene glycol (mPEG-SH) (Laysan Bio, Arab, AL) and the solution was stirred overnight. The final PEGylated rod solution was cleaned by diafiltration of the solution into DI water. The synthesized GNRs had an aspect ratio of approximately 3.42 (GNR size: 24 x 7 nm). Both GNSs and GNRs were suspended in 10% trehalose because the particles exhibit greater long-term stability in trehalose compared to PBS. In addition, 10% trehalose is iso-osmotic with blood. Figure 4.1 illustrates the normalized extinction spectra of GNSs and GNRs used in this study.

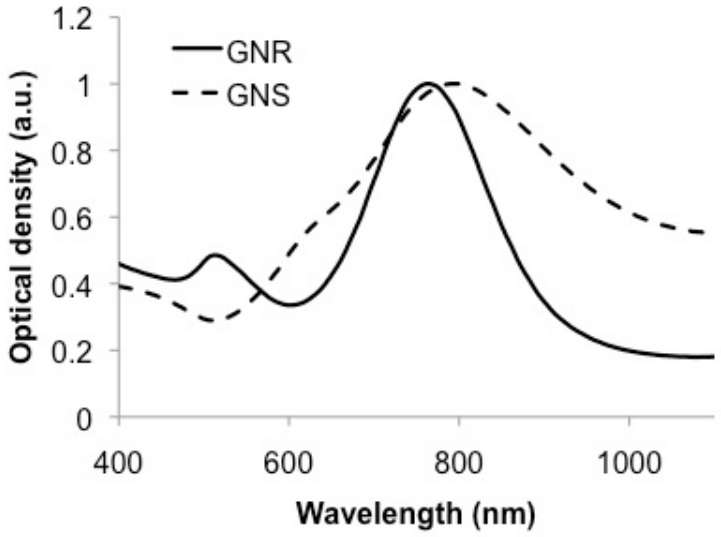

Figure 4.1: UV-VIS extinction spectra of GNSs and GNRs.

4.3.2 Cell culture and tumor inoculation in mice

A431 cells (CRL- 1555, ATCC, human epithelial carcinoma cell line) were grown in

Dulbecco's Modified Eagle's medium (30-2002, ATCC) with 10 % fetal bovine serum (30-2020, ATCC) at 37 °C under 5 % CO2. When culture reached 90 % confluency, the cells were detached from the flask by 0.25 % trypsin-EDTA (30-2101, ATCC), centrifuged, and resuspended in sterile phosphate-buffered saline (PBS). 4 to 6 week old nude mice (Swiss *nu/nu*) were inoculated with the A431 cells. Approximately 4 x 10^6 cells/50 µl were subcutaneously injected in the right thigh of the mice. When tumors attained a size of ~ 8-10 mm in diameter, we performed intravenous delivery of nanoparticles.

4.3.3 Single and multiple dosing

GNSs and GNRs solutions were intravenously injected via the mouse-tail vein for single and multiple doses at 24-hour intervals. We systemically injected nanoparticles at 24 hour intervals since this time point has shown bulk nanoparticle clearance from blood allowing maximum particle accumulation in tumors.[67, 88] We distributed 38 mice into 6 different groups. Table 1 shows the animal use for a range of doses and both particle types. Groups 1 and 2 animals received 7 µl/g of a single GNP dose (GNSs: 2.74 x 10^8 particles/ µl and GNRs: 2.005 x 10^{11} particles/ µl, optical density = 100) and were sacrificed after 24 hours followed by tumor and organ extraction for analysis. Groups (3 and 4) and Groups (5 and 6) received multiple GNP doses once per day for three days and five days consecutively at 24-hour intervals, respectively. Following the three and

five GNP doses, animals were sacrificed and the organs were extracted for analysis on the fourth and sixth day, respectively. Our control group consisted of three mice that received intravenous administration of trehalose.

Table 4.1: Number of animals utilized in each dosing group for GNSs and GNR injections.

Particle type	**Doses administered**		
	Single	Three	Five
GNS	Group 1 (n=7)	Group 3 (n=6)	Group 5 (n=6)
GNR	Group 2 (n=7)	Group 4 (n=6)	Group 6 (n=6)

4.3.4 Neutron Activation Analysis (NAA)

We performed Neutron Activation Analysis (NAA) to quantify the amount of gold present in the extracted tumors and livers from the six mice groups. NAA is the gold standard method for trace gold quantification in biological samples, with sensitivities down to 70 pg.[67] NAA was performed in the Nuclear Engineering Teaching Laboratory (NETL) at The University of Texas at Austin. Extracted tissues were weighed and placed inside the NAA vials. Following mass measurements, the vial containing tissue samples were placed in a desiccator and dehydrated for a week. Once desiccated, the vial lids were closed, and samples were sent to NETL for irradiation. From the amount of gold (mass of gold present in the samples) reported through NAA, and theoretical values for

the mass of a single GNP, we calculated the number densities of GNSs and GNRs in the tumors and livers for all animal groups. The theoretically estimated mass of a single GNS (120 nm diameter core with 15 nm shell) and GNR (24 x 7 nm) were 1.33 x 10^{-8} μg and 1.61 x 10^{-11} μg (ρ_{gold} = 19.32 g/cm^3). Additionally, to compare the percent-injected dose for GNS and GNR, the gold mass present in the injected samples (standards) were determined using NAA. Standards of GNSs and GNRs were prepared in NAA vials similar to the tissue preparation and were sent to NETL for irradiation. Based on the number of particles injected (reported from NAA of standards) and the number of particles accumulated in the tumors and livers (reported from NAA of tissue samples) for a single dose, we calculated the percent-injected dose per gram of tissue for GNSs and GNRs.

4.3.5 Histopathology

We performed histopathological analysis to determine if there was acute toxicity in tumors and in the RES organs (liver and spleen) for the mice groups that received the highest GNP dose (five doses). Liver, spleen and tumor from groups 5 and 6 was examined by a pathologist at MD Anderson Cancer Center. The tissues from groups 1 and 2 (single dose) and the control group (trehalose injected) were also examined for comparison. In addition, we obtained light microscopy images of all the groups.

4.4 Results

4.4.1 NAA – Single and multiple dosing of GNSs and GNRs

Figure 4.2 shows the accumulation of GNSs and GNRs in the tumor and liver for single, three and five doses based on NAA. These results show that three successive doses of GNPs lead to a nearly proportional accumulation in the tumors.

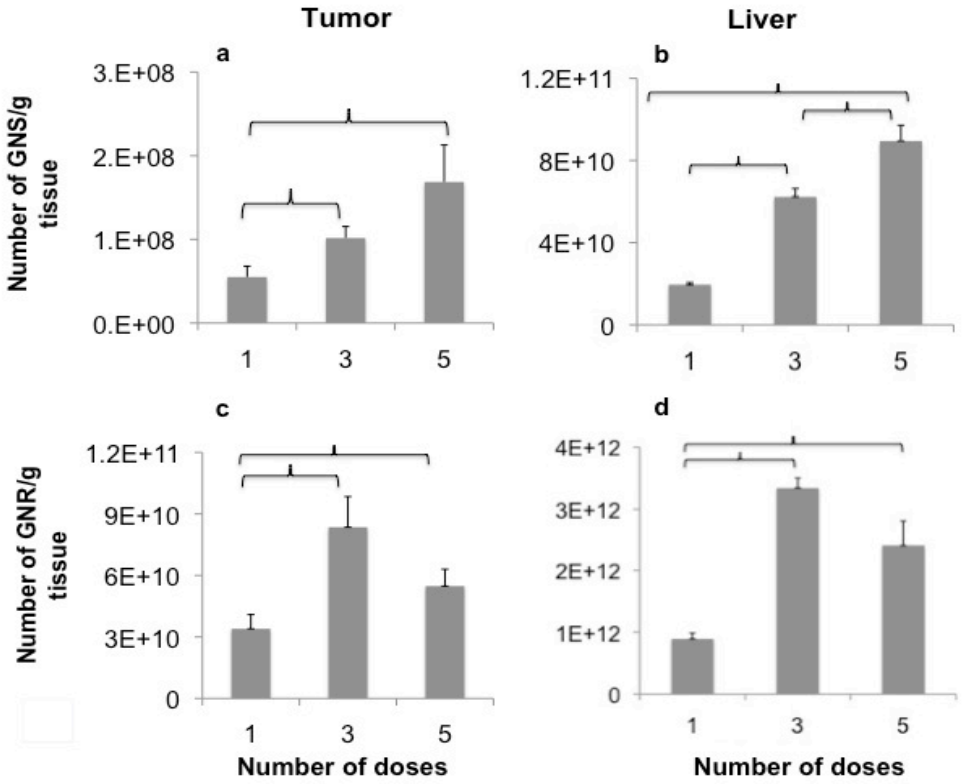

Figure 4.2: (a and b) Number density of GNSs/g of tissue for different doses (single, three and five) in tumor and liver, respectively. (c and d) Number density of GNRs/g of tissue for different doses in tumor and liver, respectively. Error bars represent standard error.

Specifically, three consecutive doses rendered approximately 2 and 2.45 times increase in particle accumulation with GNSs and GNRs, respectively (Figures 4.2a and c). However, particle accumulation in tumors receiving five consecutive doses of GNPs via the tail vein was less than expected. We observed only a 3-time increase with GNSs and 1.6-time increase with GNRs in tumors for five doses. Note that the fold increase we refer to here is relative to a single dose. In summary, we observed an increase in the number densities of GNSs and GNRs in the tumor for higher doses (three and five doses) compared to a single dose (Figures 4.2a and c). Specifically, one versus three doses and one versus five doses were statistically significant for both GNSs and GNRs. In the liver, which serves as a control, we observed a concomitant increase in number densities for GNSs with increase in doses: 3 and 4.6 times increase for three and five doses, respectively (Figure 4.2b). However, for livers accumulated with GNRs, we observed an increase in number densities from single to three doses (3 times increase) and a decrease from third to the fifth dose. However, this decrease/change was statistically insignificant. We also observed a similar, statistically insignificant decrease in the GNR tumor group.

4.4.2 NAA - Effect of particle type on tumor uptake

We observed a significant difference in tumor uptake of GNSs and GNRs for a single nanoparticle dose. Figure 4.3 illustrates the fraction of GNSs and GNRs accumulated in tumor and liver for a known injected particle dose.

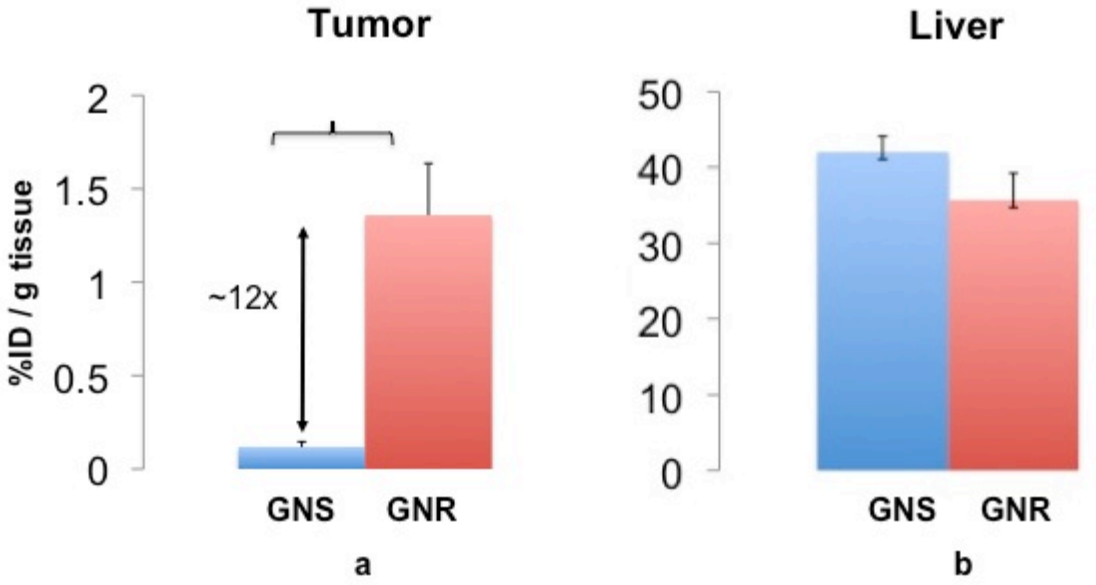

Figure 4.3: Percent injected dose per gram of tissue (%ID/ g of tissue) for GNRs and GNSs in (a) tumor and (b) liver after 24 hrs. post intravenous injection. GNRs accumulated approximately twelve times higher than GNSs in the tumor. Error bars represent standard error.

In the tumor, the smaller pegylated GNRs showed approximately 12 times higher accumulation (1.35 ± 0.29 %ID/g tissue) compared to the larger pegylated GNSs (0.118 ± 0.027 %ID/g tissue) after 24 hours. Similarly, we observed 15 and 6 times increase in percent accumulation for GNRs compared to GNSs at 72 and 120-hour time points, respectively (data not shown for 72 and 120 hour). However, in the liver, there was no statistical difference in the percent accumulation of GNSs and GNRs (GNSs: 42 ± 2.11 %ID/ g tissue, GNRs: 37 ± 3.4 ID/g tissue) at 24 hours.

4.4.4 Narrowband imaging - single and multiple dosing of GNSs and GNRs

We used NBI to image the nanoparticle distribution and accumulation pattern in A431 tumors. In addition to the heterogeneity of nanoparticle accumulation in tumor, we observed nanoparticles in close proximity to blood vessels as shown in Figure 4.4.

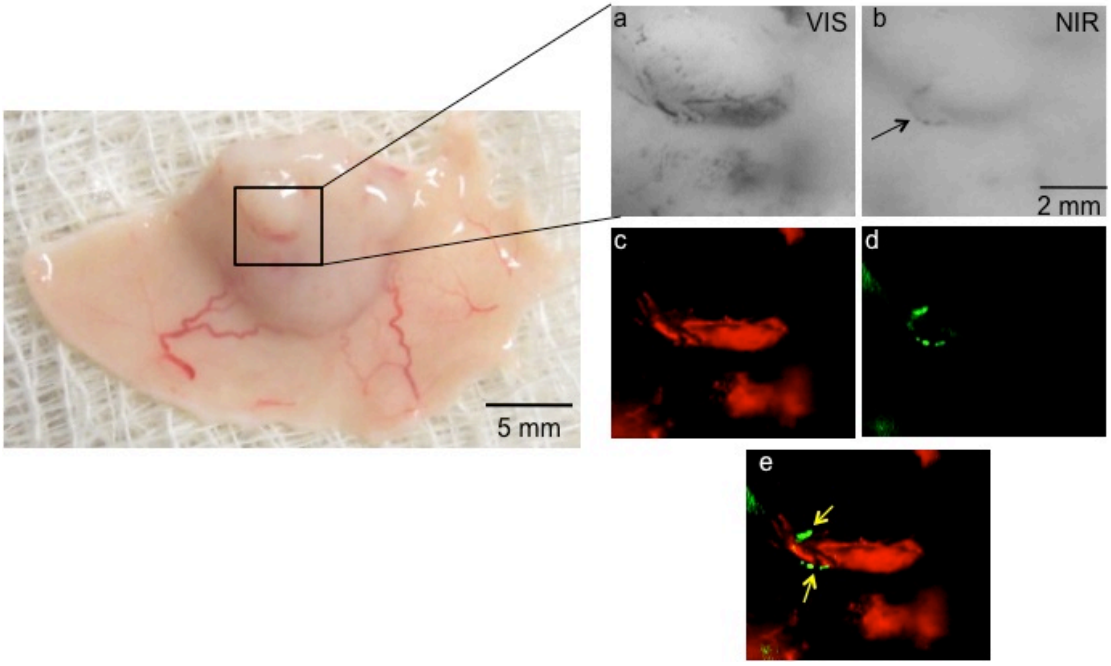

Figure 4.4. Narrow band images of GNR accumulated tumor. Nanorods are in close proximity to blood vessels. (a) VIS grayscale NBI image (b) NIR grayscale NBI image (c) VIS image inverted and assigned to red channel (d) NIR image inverted and assigned to green channel (e) composite NBi image combined using images c and d.

Figure 4.5 presents a comparison of NBI images acquired from tumors that received one and five doses of GNRs and GNSs. We did not observe any significant

differences in the accumulation profile of both particles. There was also no difference in the image contrast (due to nanoparticle labeling) provided by shells and rods.

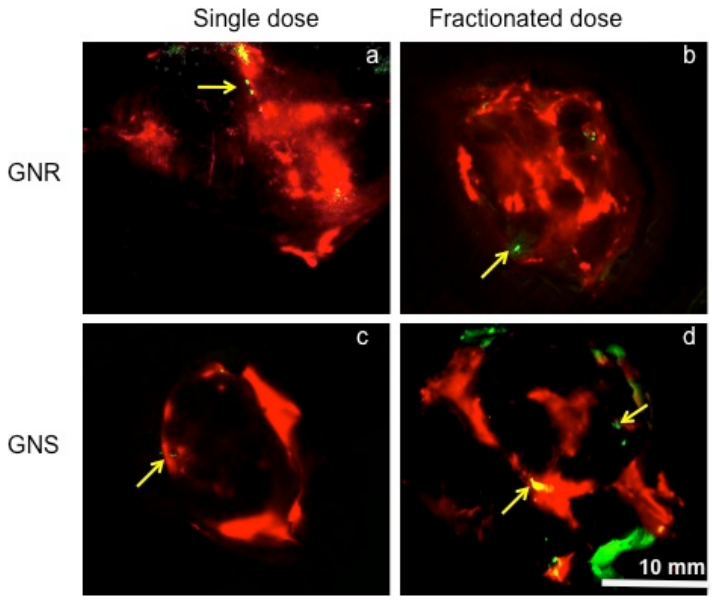

Figure 4.5. Composite NBI images of (a) and (b) single and five doses of nanorods (c) and (d) single and five doses of gold nanoshell solutions. The yellow arrows aindicate GNPs present in the tumor.

4.4.5 Histopathology of liver, spleen and tumor for multiple doses

We observed no signs of acute toxicity such as sinusoidal dilation, inflammation or necrosis in the tumor, liver and spleen for multiple doses. Figures 4.6a, b and c show light microscopy images of tumor, liver and spleen stained with H&E, respectively.

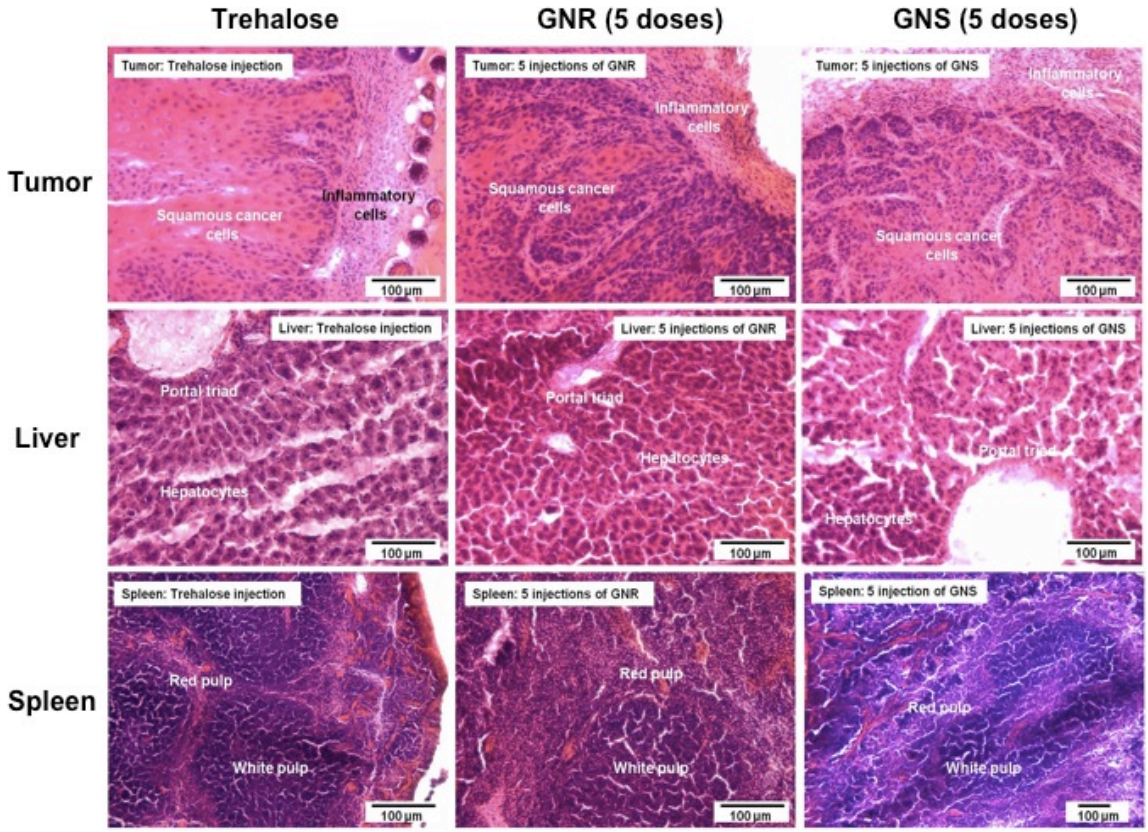

Figure 4.6: Light microscopy images of H&E stained tumor, liver and spleen from mice that received five doses of GNRs and GNR and a dose of trehalose (control).

The extent of typical inflammatory cell infiltration (lymphocytes and neutrophils) was similar in Group 1 tumors (single dose of GNSs and GNRs), Group 3 (five doses of GNSs and GNRs) and the control group (dose of trehalose). In addition, there was no appreciable difference in edema (secondary to peritumoral inflammation) between tumors of previously mentioned groups. In addition, there were no significant differences in histopathological appearance observed in the livers (Fig. 4.6b) and spleens (Fig. 4.6c) between the groups. Furthermore, in tumors, livers and spleens analyzed, there was no

histopathologically appreciable necrosis as a result of any presumed increase in microvascular blockade by aggregated GNPs, even in the group that received multiple doses of GNPs.

4.5 Discussion

In this study, we have shown that multiple dosing of gold nanoparticles injected systemically leads to a cumulative increase in particle accumulation in tumors using NAA. Multiple dosing is a common approach used in photodynamic, chemo and radiation therapies to treat tumors. In addition, multiple dosing has been shown to protract tumor growth in mouse models. In a recent study, mice bearing subcutaneous Neuro2A tumors were treated by intravenous injection with siRNA-containing nanoparticles formed with cyclodextrin-containing polycations (CDP). Three consecutive daily doses of transferrin (Tf)-targeted nanoparticles carrying two different siRNA sequences targeting ribonucleotide reductase subunit M2 (RRM2) lead to slow tumor growth.[89] The nanoparticles used in our present study are known to be effective *in vivo* tumor targeting agents.[11, 88] In addition, their strong NIR plasmon peak (Figure 4.1) enables them to scatter, absorb or luminesce when excited in the NIR.[90, 91]

Smaller particles have high permeation/diffusion through tumor interstitium and correspondingly, higher clearance to surrounding normal tissue (where they are likely to be cleared).[92] Jain *et al.* and Boucher *et al.* have shown that the interstitial fluid pressure

decreases from the tumor core to the periphery and surrounding tissue, carrying nanoparticles with it by convection into the normal tissue as a function of particle size. [93, 94] This phenomenon could explain the decrease in smaller nanoparticle accumulation in tumors with days as noted in Figure 4.2c (decreasing trend in GNR number density observed in tumors from three to five doses). In contrast, larger particles have restricted and slow migration to the tumor environment along with slow clearance from tumor owing to increased tumor accumulation with time.[86, 94] This explains the increase in GNS number density with increasing doses (more time to accumulate slowly) as seen in Figure 4.2a. However, a detailed study of the changes in nanoparticle accumulation in tumor for an extended time post single versus multiple dose delivery will help understand the mechanisms of uptake and clearance for various nanoparticle types.

We analyzed the livers of mice that received single and multiple dosing of both GNPs since liver has been shown to contain significantly higher nanoparticle accumulation compared to other RES organs.[79] The statistically significant increase in tumor accumulation of GNPs with increasing dose number in the liver (Figure 4.2b) validates the multiple dosing approaches. However, we noticed an interesting trend in the GNR group. There was a drop-off in GNR accumulation from the three-dose group to the five-dose group (Figure 4.2d). Although uptake of particles from blood to liver may occur relatively quickly, excretion of these particles from the liver is relatively slow, often resulting in prolonged retention of GNPs.[95] The decrease in GNR number density in the liver for the five-dose group, albeit statistically insignificant, is intriguing and

warrants further investigation.

Nanoparticles' size and half-life plays an important role in tumor accumulation of particles for diagnostic and therapeutic purposes. Perrault *et al.* have shown that accumulation of smaller particles (less than 40 nm) in tumors is a function of both size and half-life. For particles larger than 40 nm, the accumulation is primarily a function of half-life.[86] We used GNRs with a size of 24 x 7 nm having an approximate half-life between 4-8 hr and GNSs of 135 nm diameter with an approximate half-life of 3 hrs.[67, 88] The longer half-life and smaller size of GNRs explains their nearly 12-fold higher accumulation compared to the larger GNS.

With both particle types examined in this study, the highest tumor accumulation as a fraction of GNPs injected was only about 2%. Hobbs *et al.* have demonstrated that the vascular permeability and effective interstitial diffusion coefficient of a nanoparticle depends on the tumor type as well.[96] The relatively low accumulation fraction of both pegylated GNRs and GNSs could be attributed to the tumor type as well. Pore cut-off sizes have been measured for a limited number of tumor models with the smallest reported at 100-200 nm.[96] To our knowledge, the pore cut-off size for the squamous cell carcinoma tumors (A431 tumors) used in this study has not yet been reported. The size of the GNPs did not affect the accumulation in livers as observed in Figure 4.3b. This correlates well with prior research showing that nanoparticle accumulation in liver was irrespective of its size.[79] However, as noted in an earlier paragraph, the GNRs appear to

clear much faster from the liver after three days.

Although we noticed the effect of nanoparticle dosing strategy in tumor targeting and accumulation demonstrated using NAA, there was no effect in increase of image contrast observed through NBI (Figures 4.5). However, wide field NBI of the A431 tumors demonstrated that nanoparticles accumulated in close proximity to blood vessels. This finding has been shown previously in several other studies[46] and our diagnostic imaging tool confirmed the same. In order to use NBI combined with increased GNPs' contrast for tumor and tumor margin imaging, we intend to investigate other nanoparticle targeting strategies such as active targeting and nanoparticle delivery strategies such as *topical delivery* to effectively label and target the tumors.

The multiple dosing strategy did not lead to acute toxicity in mice during the course of the study. After administration of GNPs, mice were monitored daily for survival and behavior changes. There was no effect of fractioned dose administrations of GNPs on mortality and behavioral impairment. There were no appreciable histopathological signs of acute toxicity such as inflammation, edema, sinusoidal dilation and necrosis in all mice groups. Further studies are required to ascertain the effect of multiple dosing on long-term clearance, safety and biodistribution. Multiple dosing could potentially improve thermal therapy efficacy as the number densities accumulated in the tumor increased for higher doses compared to a single dose.

Chapter 5

Topical delivery of antibody conjugated gold nanorods

5.1 Introduction

Squamous cell carcinoma (SCC) is the second-most common skin cancer after basal cell carcinoma (BCC) with over 250,000 new cases detected every year.[97] However, SCCs are more likely to be aggressive and invade the dermal skin layers. Recently, several optical imaging techniques have been developed to enable rapid detection of non-melanoma skin cancers noninvasively in surgical skin excisions. The techniques include multispectral fluorescence polarization,[98, 99] confocal reflectance microscopy,[18, 100, 101] optical coherence tomography[102, 103] and fluorescence spectroscopy.[104] Several of these imaging methods have utilized extrinsic contrast agents

such as acetic acid, methylene blue and toluidine blue dyes to enhance contrast of the SCC tumor relative to the surrounding normal tissue.

NIR-absorbing GNRs have considerable advantages over molecular dyes and fluorophores as contrast agents for NIR imaging applications. GNRs have tunable optical properties and high optical absorption cross sections in the NIR region, making them attractive probes for *in vitro* and *in vivo* imaging.[38, 105] As described in previous chapters, nanoparticles when injected systemically or intravascularly, extravasate from the leaky neovasculature and accumulate in tumors due to the EPR effect. In an effort to increase targeting contrast, recent efforts have focused on active targeting strategies, wherein the nanoparticles' surface is functionalized with antibodies to specifically target tumors.[42-44] Loo *et al.* demonstrated active targeting using anti-HER2 conjugated gold nanoshells to image breast carcinoma cells.[106] El Sayed *et al.* have demonstrated active targeting of both nanospheres and nanorods using anti-EGFR antibodies *in vitro.* [53, 54] However, even with the systemic delivery of these particles, only a small percentage (~2%) of the administered nanoparticles reach the tumor target [67], and the residual material may raise concerns for toxicity and inadequate clearance from the body.

To improve the percentage of nanoparticles delivered to tumors and reduce the quantity accumulating in vital organs, we *topically* applied antibody conjugated GNRs on tumor xenograft models and imaged using NBI. Recently, several research groups have used this delivery technique to specifically target disease tissues. Nitin *et al.* evaluated

the fluorescence contrast properties following topical delivery of 2-[N-(7-nitrobenz-2-oxa-1,3-diazol-4-yl) amino]-2-deoxy-glucose (2-NBDG) in freshly resected clinical specimens of neoplastic oral mucosa using fluorescence imaging. [107] Bickford *et al.* used gold nanoshells as rapid diagnostic agents for imaging human breast tissue sections that over-expressed HER2 receptors. [65, 108]

We targeted the epidermal growth factor receptor (EGFR) over-expressed in SCCs (A431 cancer cells) using GNRs conjugated to Cetuximab (C225, a humanized anti-EGFR antibody that is currently approved for clinical use). EGFR is a transmembrane receptor tyrosine kinase stimulated by growth factors, such as transforming growth factor (TGF)-α or EGF, that binds to the extracellular domain of the receptor.[109] EGFR promotes multiple tumorigenic processes, stimulating proliferation, angiogenesis and metastasis as well as protecting cells from apoptosis.[110] EGFR is a viable molecular target that has been shown to highly over-express in several skin SCCs.[111, 112] Several groups have used EGFR as probes to target, image and treat A431 cells and tumor xenografts. Durr *et al.* used anti-EGFR antibody conjugated nanorods to detect and image A431 skin cancer cells embedded in a three-dimensional tissue scaffold using two-photon luminescence (TPL) microscopy.[113] Recently, Melancon *et al.* used anti-EGFR antibody conjugated hollow gold nanoshells to target A431 cells *in vitro* and *in vivo* and performed photo-thermal ablation of cells *in vitro*.[114]

In this chapter, we present the results of a study exploring the feasibility of topical administration of anti-EGFR antibody conjugated GNRs (C225-GNRs) on A431 tumor cross-sections to target EGFR. We imaged tumor cross-sections topically administered with both C225-GNRs and pegylated GNRs (control) using NBI. We show that C225-GNRs provided significantly higher tumor contrast compared to non-targeted pegylated GNRs (PEG-GNRs). In addition, we determined the penetration depth of the topically administered C225-GNRs and confirmed their binding affinity in tumors using two-photon microscopy (TPM).

5.2 Materials and Methods

5.2.1 Bioconjugation of GNRs to Cetuximab (C225-GNRs)

The synthesis of pegylated GNRs was carried according to the method of Jana et al. and has been described in Chapter 3. We adopted a three-step process for the bioconjugation of GNRs to Cetuximab. Our synthesis protocol utilizes the classical thiol-maleimide chemistry and the details of the conjugation process are as follows:

Step-1: Functionalization of GNRs with PEG: Prior to conjugation the CTAB coated GNRs were briefly sonicated to disperse the GNRs in to a homogenous suspension. Methoxy-PEG-thiol (monofunctional PEG; mPEG-SH2K) and PEG bis Thiol (bifunctional PEG; SH-PEG5K-SH) were mixed in the ratio of 4:1 to arrive at a final concentration of 2mM. The freshly made PEG solution was mixed with clean GNRs in

the ratio of 1:9, stirred thoroughly and incubated for 1-2 hrs at room temperature, with gentle shaking. At the end of the incubation time the GNRs were centrifuged at 10,000 rpm for 20 minutes to remove the unreacted PEG and the pellets were resuspended in PBS to form a uniform suspension of PEG-GNRs, with the terminal thiol (-SH) group at one end of the bifunctional PEG available for further conjugation with anitbody.

Step-2: Activation of antibody: Cetuximab® (152 kDa), an anti-epidermal growth factor receptor (EGFR) antibody, is activated by reacting with a heterobifunctional crosslinker, succinimidyl 4-[N-maleimidomethyl] cyclohexane-1-carboxylate (SMCC; MW 334.32; arm length 0.83 nm) to expose the maleimide groups for the subsequent conjugation with PEG-GNRs containing free thiol (-SH) moieties. Approximately 20-fold molar excess of SMCC was added to the antibody solution (2mg/ml) and incubated for 2 hrs at 4 °C. At the end of the reaction, the unbound cross linker molecules were removed by eluting the reaction mixture through a desalting column and the purified maleimide-activated Cetuximab was collected in a clean tube for further reaction with PEG-GNR.

Step-3: Conjugation of Cetuximab® to GNRs: The maleimide-activated Cetuximab (prepared from Step-2) was mixed with the PEG-GNRs with free thiol moieties (prepared from Step-1) such that the final concentration of maleimide-activated Cetuximab is ~ 10 μg/ml. After overnight reaction at 4 °C, the unbound antibody was removed by centrifugation at 10,000 rpm for 20 minutes. The centrifugation step was repeated three times and the pellets were collected and reconstituted in sterile phosphate

buffered solution (PBS). The optical density of both PEG-GNRs (plasmon resonance peak @ 776 nm) and C225-GNRs (plasmon resonance peak @ 754 nm) was measured using UV-Vis spectrophotometer (Beckman Coulter DU720, Brea, CA) and their normalized extinction spectra are shown in Figure 5.1.

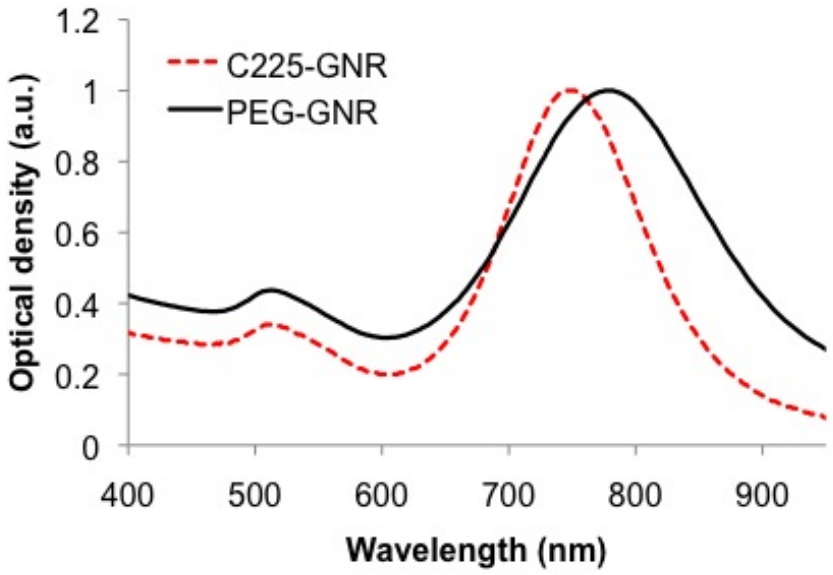

Figure 5.1: UV-VIS extinction spectrum of PEG-GNRs and C225-GNRs.

The conjugation efficiency was evaluated by measuring the zeta (ζ) potential of the final conjugates. The CTAB coated GNRs used at the beginning of the conjugation process showed a zeta potential in the range +60 to +80 mV. After the functionalization of GNRs with SH-PEG the zeta potential decreased to +5 to +10 mV. With the addition of Cetuximab® to GNRs, the zeta potential further decreased and reached near neutral values in the range of +4 to -5 mV. These values were consistent among different

conjugation batches indicating the efficiency of surface functionalization and Cetuximab® conjugation to the surface of GNRs. Finally the conjugation efficiency was validated using protein assay by quantifying the ratio of Cetuximab® to GNR. Prior to the protein estimation the optical density (OD) of PEG-GNRs and C225-GNRs at the assay readout wavelength was adjusted to the same value. PEG-GNRs and C225-GNRs were subjected to assay protocol and the assay end product was measured. With the known values of GNR/ml ($2x10^{11}$ GNR/ml at 1 OD) and the measured concentration of C225 in the C225-GNR samples, the ratio of C225 molecules per GNR was estimated as ~110 - 140 C225 molecules/GNR.

5.2.3 *Ex vivo* mouse skin tumor tissues

A431 cells (CRL- 1555, ATCC, human epithelial carcinoma cell line) were grown in Dulbecco's Modified Eagle's medium (30-2002, ATCC) with 10 % fetal bovine serum (30-2020, ATCC) at 37 °C under 5 % CO2. When culture reached 90 % confluency, the cells were detached from the flask by 0.25 % trypsin-EDTA (30-2101, ATCC), centrifuged, and re-suspended in sterile phosphate-buffered saline (PBS). Approximately 4 x 106 cells/50 µl were subcutaneously injected in the right thigh of 4 to 5 week old nude mice (Swiss nu/nu). When tumors attained a size of ~ 8-10 mm in diameter, we sacrificed the mice and excised the tumors for topical delivery of GNRs followed by imaging.

5.2.4 Topical delivery of PEG-GNRs and C225-GNRs

We performed topical delivery of both PEG-GNRs and C225-GNRs on A431 tumor cross-sections. The tumor sections were divided into the following two groups: 1) Group 1 tumor cross-sections (n=6) received a topical delivery of 60 μl of PEG-GNRs and was designated the control group; 2) Group 2 tumor cross-sections (n=6) received 60 μl of C225-GNRs. The optical density of PEG-GNR solution was matched to that of C225-GNR (OD = 25) by diluting in PBS before topically applying on tumors. Because PEG-GNRs have no targeting moiety, they are treated as the control group in our experiments. Prior to nanoparticle delivery baseline NBI images were acquired. Following baseline imaging, the tumor cross-sections were incubated with PEG-GNRs or C225-GNRs for 30 minutes at 37 °C under 5 % CO_2. At the end of incubation time, the tissues were washed three times with 1X PBS for NBI and two-photon microscopy.

5.2.5 Two-photon microscopy

We performed two-photon microscopy of the tumor samples incubated with C225-GNRs and PEG-GNRs using a custom-built NIR laser scanning multiphoton microscope described previously [115]. Briefly, we used a femtosecond Ti: Sapphire laser (Mira 900 with excitation wavelength of 800 nm; Coherent, Inc., Santa Clara, CA) as the excitation

source, and the laser beam was raster scanned along the sample using a pair of galvanometric scanning mirrors (6215HB; Cambridge Technology, Inc., Lexington, MA) to produce 2D images. We detected the two-photon luminescence from the GNRs using two photomultiplier tubes (PMT) (H7422P- 40, H7422P-50; Hammamtsu Corporation, Bridgewater, NJ) through a dichroic beam splitter (FF735-Di01; Semrock, Inc., Rochester, NY). We applied an incident laser power of 40.8 mW and band pass filtering of 6 dB gain. In order to determine the penetration depth of the GNRs, we obtained images (512 x 512 pixels) in the z-direction and created a stack of images to analyze the particle penetration as a function of depth.

5.3 Results

5.3.1 NBI of A431 tumors topically administered with PEG-GNRs

Figure 5.2 presents a qualitative assessment of tumor cross-sections incubated with the control PEG-GNRs. The images show no perceivable contrast in the NIR using NBI. The red color in the NBI images corresponds to blood. We did not observe any PEG-GNRs in the post delivery NIR NBI images after the PBS wash (Fig. 5.2f).

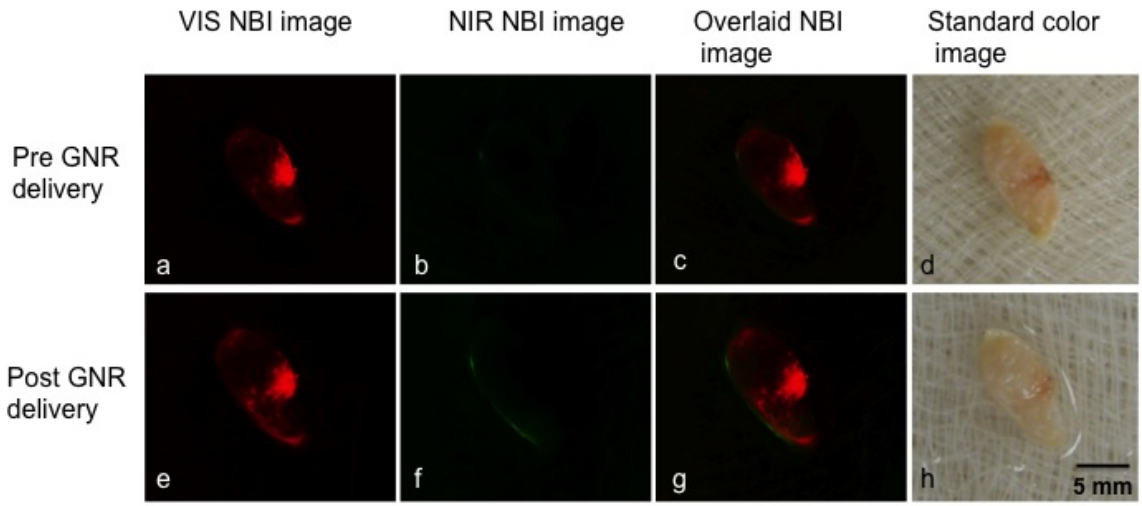

Figure 5.2: Images of EGFR over-expressing A431 tumor cross-sections captured before and after the incubation of PEG-GNRs. (a, b, and c) VIS, NIR and overlaid NBI images of A431 tumors before incubation with PEG-GNRs, respectively. (d) Corresponding standard color image of tumor cross-section. (e, f and g) VIS, NIR and composite narrow-band imaging images of A431 tumors incubated with PEG-GNRs for 30 min. at 37°C, respectively. (h) Corresponding standard color image of tumor cross-section incubated with PEG-GNRs. The red color in the NBI images corresponds to blood.

5.3.2 NBI of A431 tumors topically administered with C225-GNRs

Figure 5.3 demonstrates that tumors incubated with GNRs targeted specifically to tumor growth factor receptors (bottom row) resulted in a significantly higher image contrast compared to the untargeted tumor (top row) as shown in Figure 5.3.

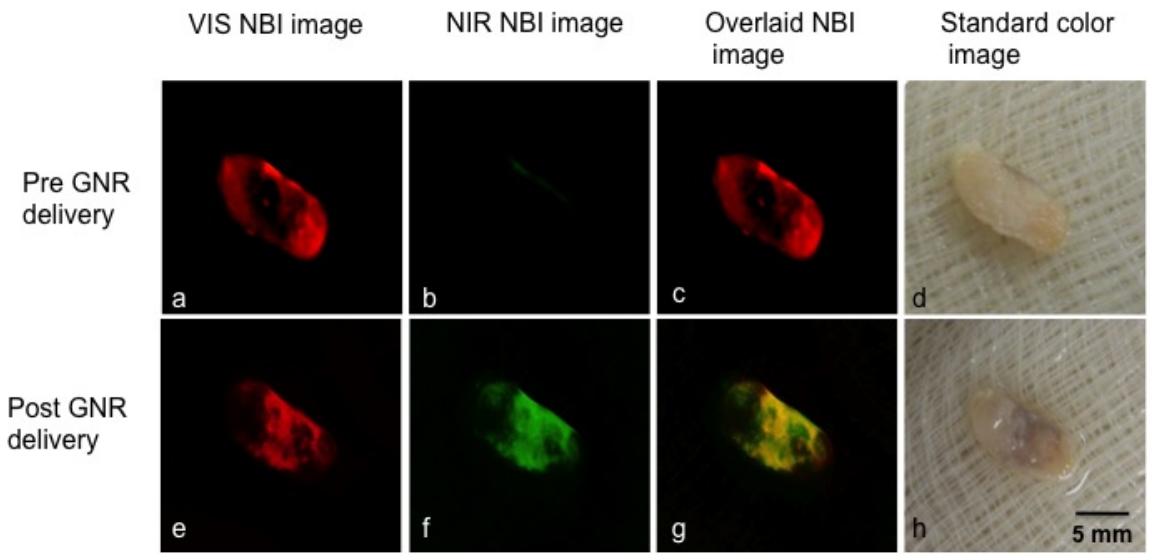

Figure 5.3: Images of EGFR over-expressing A431 tumor cross-sections incubated with and without C225-GNRs. (a, b, and c) VIS, NIR and overlaid NBI images of A431 tumors before incubation with C225-GNRs, respectively. (d) Corresponding standard color image of tumor cross-section. (e, f and g) VIS, NIR and composite NBI images of A431 tumors incubated with C225-GNRs for 30 min. at 37°C, respectively. (h) Corresponding standard color image of tumor cross-section incubated with C225-GNRs. The red color in the NBI images corresponds to blood and the green color corresponds to C225-GNRs attached to EGFRs expressed on A431 tumors.

The red color in the NBI images corresponds to blood and the green color corresponds to EGFR-targeted GNRs attached to EGFRs expressed on A431 tumors. The composite NBI images of tumors demonstrated that GNRs targeted specifically to tumor growth factors resulted in higher nanorod binding to tumor receptors and a significantly higher image contrast compared to non-targeted gold nanorods (PEG-GNR). In addition, the NBI images highlight the regions of C225-GNR binding to the tumor receptors compared to the standard color images (Fig 5.4).

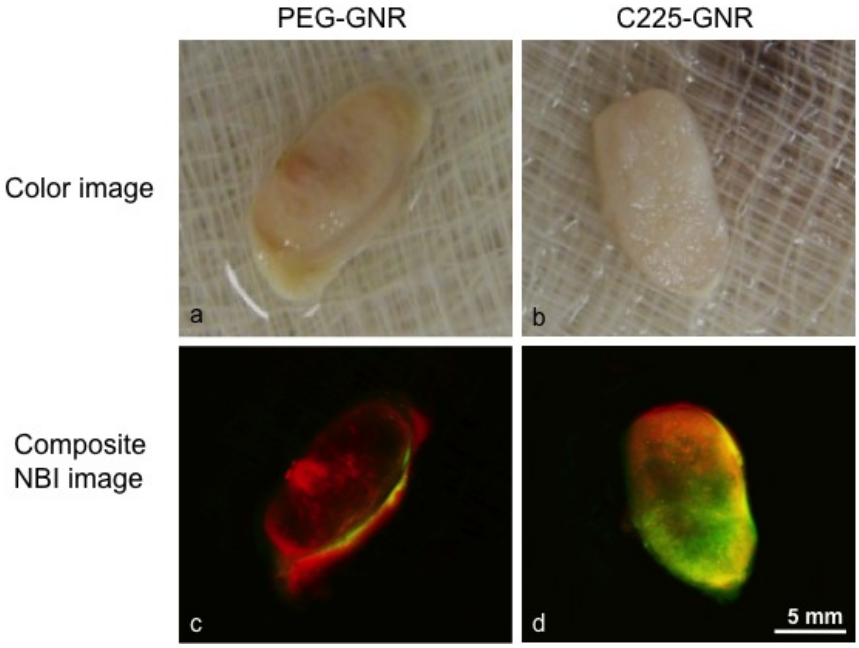

Figure 5.4: Images of EGFR over-expressing A431 tumor cross-sections incubated with PEG-GNRs and C225-GNR for 30 min. at 37°C. (a and b) Standard color images of A431 tumor cross-sections incubated with PEG-GNR and C225-GNR, respectively. (c and d) Corresponding composite near-infrared NBI images of A431 tumor cross-sections incubated with PEG-GNRs and C225-GNRs, respectively. The red color in the composite NBI images corresponds to blood and the green color corresponds to C225-GNRs attached to EGFRs expressed on A431 tumors.

5.3.3 Quantitative analysis of tumor cross sections incubated with GNRs

We quantified the image contrast obtained with tumor images from both experimental groups. Prior to topical application of GNRs, there was no significant difference in mean reflectance intensity between C225- and PEG-GNR treated tumors. As seen in the images from Figure 5.2, a topical application of PEG-GNRs did not lead to an improvement in image contrast; the mean reflectance intensity was nearly the same as the baseline measure. However, the mean reflectance intensity from tumors treated with C225-GNR

was approximately 2.5 times higher than the reflectance from tumors treated with PEG-GNRs ($p < 0.05$) as shown in Figure 5.5.

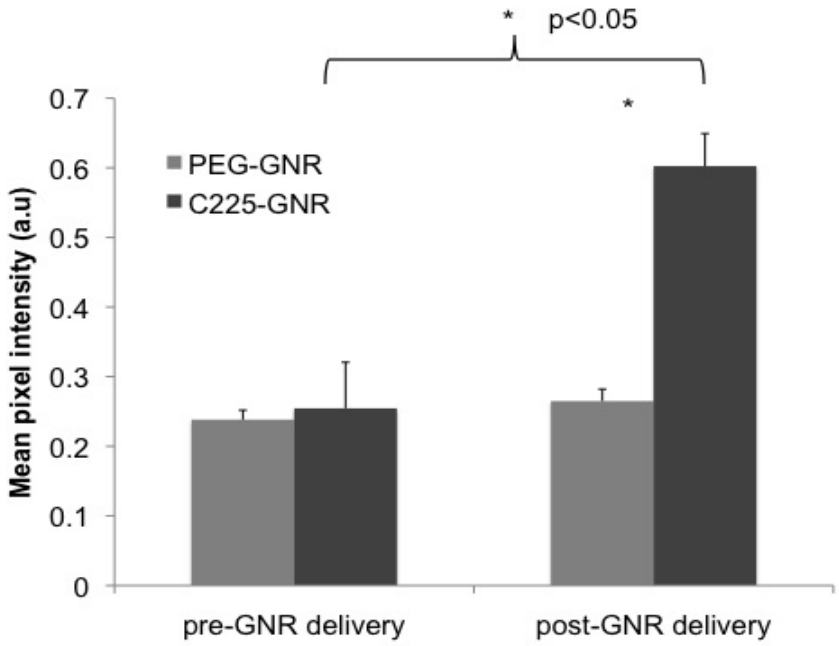

Figure 5.5: Mean intensity values for samples of A431 tumors incubated with PEG-GNRs and C225-GNRs. Differences between EGFR over-expressing tumor incubated with PEG conjugated GNRs and EGFR-targeted GNRs was statistically significant ($P < 0.05$, $n = 6$). Differences between the post and pre C225-GNR delivery and incubation was statistically significant ($P < 0.05$, $n = 6$). Error bars represent standard deviations.

5.3.4 Two-photon imaging demonstrating EGFR binding of C225-GNRs

We performed two-photon microscopy of the tumor samples incubated with both PEG-GNR and C225-GNR to microscopically demonstrate the binding of EGFR targeted GNR in tumors and to study their depth profile. Figures 5.6a and b represent cross-sectional view of z-projected images of PEG-GNRs and C225-GNRs incubated tumors,

respectively. Panels c – f represent *en-face* two-photon images of PEG-GNRs and C225-GNRs-incubated tumors obtained at different depths. C225-GNRs were mostly observed at depths of up to 300 μm from the tumor surface as seen in Figure 5.6b. On the other hand, we observed only traces of PEG-GNRs in the control image. A large proportion of signal in the control image can be attributed to instrument noise. This background signal is also visible in the C225-GNR image (Panel f) at 300 μm. The two-photon images of targeted GNR confirmed the specificity of C225-GNRs and their binding affinity to the EGF receptors over expressed in the A431 tumors.

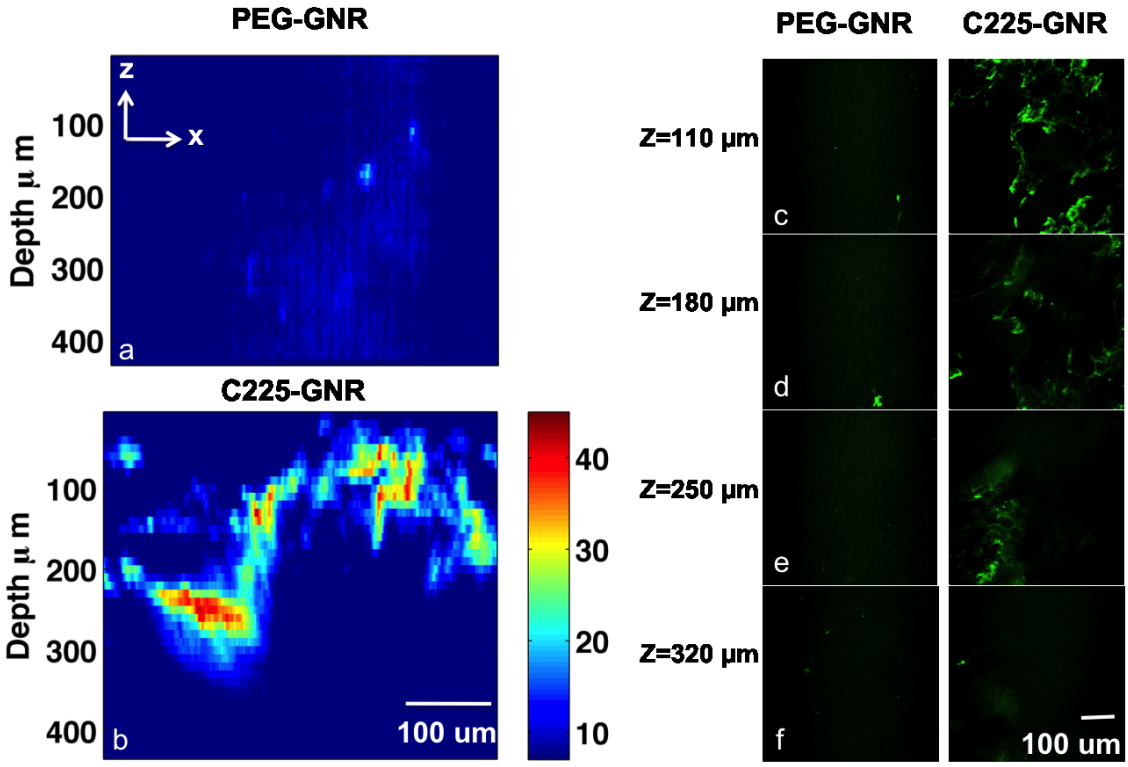

Figure 5.6: (a, b) Cross-sectional view of z-projected images of PEG-GNRs and C225-GNRs incubated tumors. (c – f) *en-face* two-photon images of PEG-GNRs and C225-GNRs accumulated tumors obtained at different depths. C225-GNRs were observed to have maximum accumulation at a depth greater than 100 µm below the tumor surface. Figures 5.6a and b are on the same scale.

5.4 Discussion

In this study, we have shown that anti-EGFR antibody conjugated GNRs combined with near-infrared NBI could yield significant contrast for optical imaging of squamous cell carcinoma tumors. We used GNRs conjugated to antibody Cetuximab® (C225) for targeting EGFRs over-expressed in SCC tumors. The antibody conjugation on the GNRs resulted in a 22 nm blue shift in the extinction maximum as seen in Fig 5.1. The shift in

the plasmon resonance peak is possibly due to the change in the local refractive index resulting from antibody conjugation [116]. However, the plasmon peak shift did not hinder imaging of both PEG-GNRs and C225-GNRs due to the optimum bandwidth of the NIR band pass filter utilized.

Topically delivered anti-EGFR antibody conjugated GNRs provided enhanced visualization of A431 tumors using NIR NBI. The topical delivery method is a non-invasive approach and can potentially reduce the interaction of particles with untargeted tissues. We have shown that GNRs targeted to EGFR significantly highlight the tumor tissue in the near-infrared NBI image (Fig 5.4f) compared to the NBI images of untargeted PEG-GNRs (Fig 5.3f). We observed that a small quantity (60 μl) of C225-GNR delivered topically, is sufficient to produce substantial contrast in the images, suggesting that this delivery technique can reduce the amount of nanoparticles required for imaging applications. Recently, Aaron *et al.* demonstrated molecular binding of topically delivered anti-EGFR gold conjugates on human cervical biopsies and imaged EGFR using reflectance confocal microscopy.[117] Bickford *et al.* have shown that topically administrated targeted gold nanoshells could help detect HER-2 over-expressing cells in human breast tissue sections using reflectance confocal microscopy.[108] In addition, Nitin *et al.* evaluated the optical contrast achieved after topical delivery of EGF-Alexa 647 that targeted EGFR in oral lesions using wide-field fluorescence imaging. [107] To our knowledge, we show the first absorption based wide field optical imaging of anti-EGFR antibody conjugated GNRs targeted to EGFR in SCC tumors. We could

potentially combine the effectiveness of the topical delivery method with wide-field NBI to aid in tumor and tumor margin detection during Mohs surgery.

The near-infrared and composite NBI images of tumors incubated with C225-GNRs demonstrated enhanced contrast of the tumors due to the binding of C225 to the EGF receptors. In addition, the comparison of color images and composite NBI images in Fig 5.5 demonstrated the utility of NIR NBI for better visualization of targeted tumors. We have used gold nanoparticles as contrast agent because they produce localized heating and could cause destruction of cancer cells when irradiated by a NIR laser at their plasmon peak.[57] The NBI platform combined with targeted gold nanorods could potentially guide precise photo-thermal therapy without causing damage to surrounding normal tissue. Although we have used NIR absorbing GNRs for imaging the SCC tumors, one could also use NIR fluorophores targeted to EGFR and image using the NBI technique.

Using two-photon microscopy, we evaluated the surface labeling as well as the potential penetration depth of the EGFR-targeted nanorods. Recently, two-photon microscopy has been used to demonstrate effective binding of anti-EGFR GNRs in A431 cells [113] and anti-HER2 gold nanoshells in breast cancer cells. [65] The two-photon images of PEG-GNRs in Figs. 5.7 a, c-f (left columns) demonstrated that there is minimal effect of passive targeting (diffusion-mediated transport). We observed C225-GNRs at depths greater than 100 μm in the tumors. We believe this large penetration depth could be the

result of the long incubation time used in the study. Due to the excellent levels of EGF binding at the current incubation times, we plan to determine the shortest incubation time that can still provide good image contrast.

Our results suggest that EGFR could be used as a molecular marker for the assessment of SCC tumors and potentially its margins. Therefore, it is important to understand the distribution of EGF receptors throughout the tumor tissue. We observed a homogenous distribution of the conjugated nanorods on the tumors due to the topical delivery approach. The tumor microenvironment has vascular abnormalities and poor lymphatics leading to high interstitial fluid pressure. [118] This interstitial hypertension restricts nanoparticle penetration into the tumor core when injected systemically, leading to a heterogeneous distribution in the tumor periphery.[72] However, we believe that the topical delivery approach could help achieve a uniform nanoparticle distribution in tumors. The homogenous distribution of GNRs suggests that this accumulation profile could benefit bulk tumor therapy directed through drugs or photo-thermal ablation.

Chapter 6

In vivo real-time imaging of breast and pancreatic tumor margins

6.1 Motivation

This chapter presents ongoing work using the second-generation NIR NBI system. The real-time system developed in Chapter 4 is used in *ex vivo* and *in vivo* settings to identify tumor margins. This chapter represents a culmination of our efforts towards building a portable, clinically compatible, real-time system for imaging tumor margins by exploiting exogenous contrast from nanoparticles. We also present an additional component that can help perform photo thermal therapy on the tumors. We have performed our studies on

two cancer models that best represent the urgent need for a real-time intraoperative surgical guidance tool – breast and pancreatic cancer.

6.2 Introduction

Most breast cancer patients have surgery to remove the tumor from the breast. The main purpose of breast conservation surgery is to remove the entire tumor and obtain clear margins around the cavity to decrease the chance of local tumor recurrence. However there are challenges identifying the residual tumor at the margin. Therefore, techniques that aid in identifying positive surgical margins intraoperatively may have a significant impact on survival and disease progression.

For all stages of pancreatic cancer combined, the 5-year survival rate remains at a low 5%, making it the most lethal of all solid tumors.[119] Only about 10% of patients are presented with resectable disease and are suitable for potentially curative surgery.[120] Even for patients who are qualified for surgery, aggressive metastasis often occurs after the operation since there are technical challenges identifying the resection margin status during surgery.

In this chapter, we present preliminary experiments conducted to determine feasibility of *ex vivo* and *in vivo* imaging of a breast tumor model that received both systemic and topical delivery of PEG-GNRs and antibody conjugated GNRs. We also present initial feasibility to evaluate the efficacy of real-time NBI combined with photo

thermal ablation to treat positive pancreatic tumor margins in a small cohort of mice. We performed *ex vivo* and *in vivo* NIR NBI of the pancreatic tumor margins accumulated with systemically injected pegylated and conjugated GNSs.

6.2 Materials and methods:

The imaging and photo thermal ablation of tumors were carried out at Nanospectra Biosciences Inc. and MD Anderson Cancer Center in Houston, TX.

6.2.1 MCF-7 breast cancer line

We used female *Fox 1^{nu}* mice inoculated in the mammary fat pad and flank with breast cancer cells (MCF-7). Tumors sizes were measured regularly and reached ranges between 3 – 5 mm over 3 months. The mouse received 4.5μL/g of GNR solution normalized to an optical density of 52 at 800nm injected intravenously via the tail vein. The mouse was sacrificed 24hr following GNR injection, and the bulk tissue containing the tumor was resected from the mouse. We imaged 3 flank tumors and 2 mammary fat pad tumors from a total of four mice (n=4) using NIR NBI.

For *in vivo* imaging, we brought the NBI system from UT Austin to Nanospectra Biosciences facility. We performed *in vivo* narrow band imaging of MCF-7 breast tumors that received systemic injections (n=3) and topical administration (n=3) of PEG-GNRs and folic acid conjugated GNRs. The mice were anesthetized using the approved

ketamine/xylazine/acepromazine cocktail. An incision was made in the skin of the flank, exposing the subcutaneous tumor and cross-section for imaging.

For topical delivery, we administered 200 μL of the conjugated nanorod suspension (optical density = 5) with plasmon resonance peak at 772 nm. After 30 minutes, we washed the tumor cross-sections and surrounding tissue thrice with 1X PBS. The tumor cross-sections along with the surrounding normal tissue were imaged *in vivo* using NBI.

6.2.2 MiaPaCa- 2 pancreatic tumor model

The animal model was developed at the MD Anderson Cancer Center research facility at Houston. Luciferase transfected MIAPaCa-2 cells were subcutaneously injected in the right flank of nude mice. Once the required tumor size (8-10 mm) was reached, GNSs were systemically injected. After 24 hrs, the mice were anesthesized and received luciferin (150 mg/kg i.p) 10 min prior to imaging. Ten minutes after luciferin injection, bioluminescence was measured using the IVIS imaging system (Xenogen corporation, US) to detect viable cancer cells. An incision was made on the skin overlying the tumor to expose the tumor. The exposed tumor was resected leaving positive margins or residuals. The surgical bed with positive margins was re-imaged using both bioluminescence imaging and NBI.

6.2.3 Evaluation of *ex vivo* and *in vivo* NIR NBI of pancreatic tumor margins

A pancreatic cancer xenograft model of minimal residual disease (MRD) was established to perform NIR NBI. In collaboration with researchers at MD Anderson Cancer Center, we established an animal model with MRD to mimic positive resection margins of pancreatic cancer. This model represented residual disease after surgery and/or inoperable pancreatic cancer identified at the time of surgery. In general, surgeons remove as much tumor at the retroperitoneal margin as technically feasible. Any further resection is generally unsafe due to fear of denervating the bowel by injuring nerves running along the vessels along this margin.

We used a small group of mice (n=6) to test the feasibility of the minimal residual disease model *ex vivo*. Animals were randomly distributed in three groups: a) control group (n=2), b) untargeted pegylated gold nanoshells injected (n=2), and c) RGD conjugated gold nanoshells injected mice (n=2). After 24 hrs following gold nanoparticle and trehalose delivery, the MRD was established followed by bioluminescence imaging. The mice were euthanized and the tumors excised for imaging.

For in *vivo* imaging, eleven animals were randomly distributed in three groups: a) control group (n=5) (trehalose injected and laser treated), b) untargeted PEG-GNSs systemically injected and laser treated (n=2), and c) RGD conjugated gold nanoshells systemically injected and laser treated (n=4). After 24 hrs following gold nanoparticle and trehalose delivery, the mice were anesthetized using the approved

ketamine/xylazine/acepromazine cocktail and the MRD was established followed by bioluminescence and NIR NBI.

6.2.4 Combined NBI and thermal ablation setup

We evaluated the initial feasibility to perform image-guided photothermal therapy of the residual tumors. We combined a laser with the second generation NBI system to perform image-guided surgery of pancreatic tumor margins. Laser irradiation was performed using a NIR diode laser for 3 min. (808 nm and 4 mW/cm^2). The temperature increase was monitored using a temperature sensor. Figure 1 shows the combined system for *in vivo* image guided therapy of pancreatic tumor margins in a mouse model.

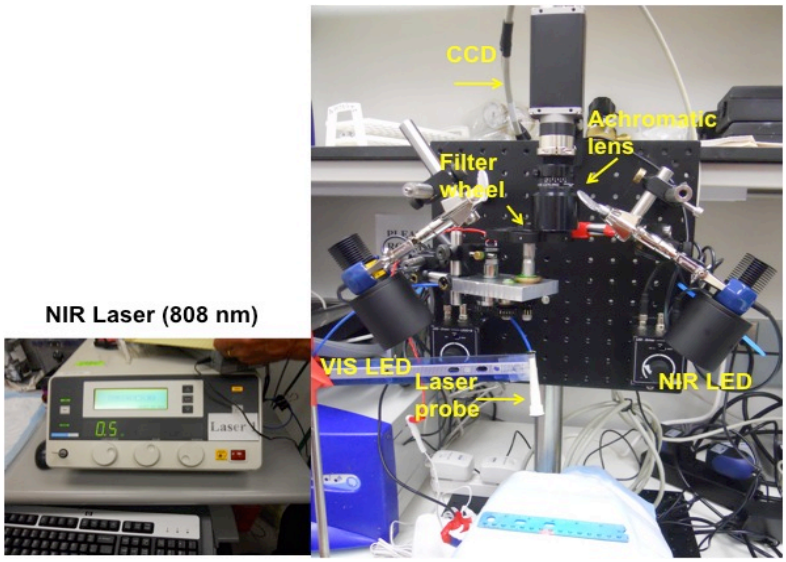

Figure 6.1: Combined system for *in vivo* image guided therapy of pancreatic tumor margins in a mouse model.

6.3 Results

6.3.1 *Ex vivo* imaging of gold nanorods in MCF-7 tumor

Figure 6.2 shows representative images of the flank tumor imaged using NIR NBI. The images demonstrated the feasibility of imaging GNRs in MCF-7 tumors using NIR NBI. However, we observed GNRs only in only one out of three flank tumors.

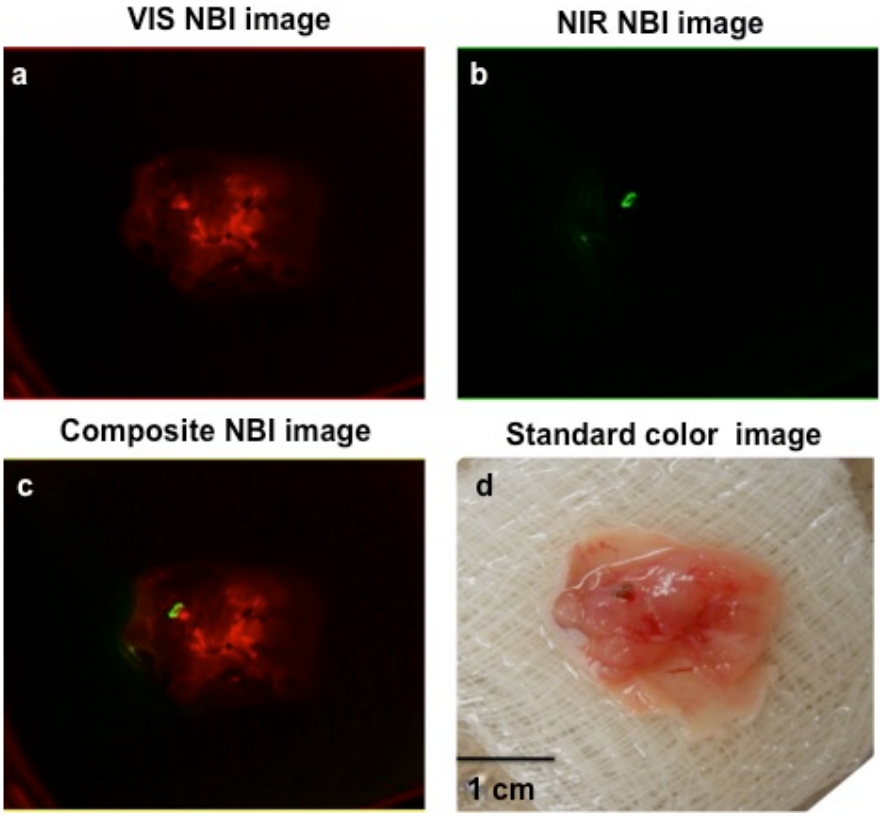

Figure 6.2. *Ex vivo* images of a MCF-7 flank tumor a) Narrow band VIS image assigned to red channel, b) Narrow band NIR image assigned to green channel, c) Composite NBI image, and d) Standard color image.

6.3.2 *In vivo* imaging of gold nanorods in MCF-7 tumors

Figure 6.3 demonstrates *in vivo* imaging of MCF-7 tumor cross-sections accumulated with PEG-GNRs using NBI. GNRs were not detected on the superficial tumor capsule of any of the three viewed tumors. Therefore, we sliced each tumor transversely exposing the cross-section for imaging. We observed nanorod accumulation in one out of three tumors.

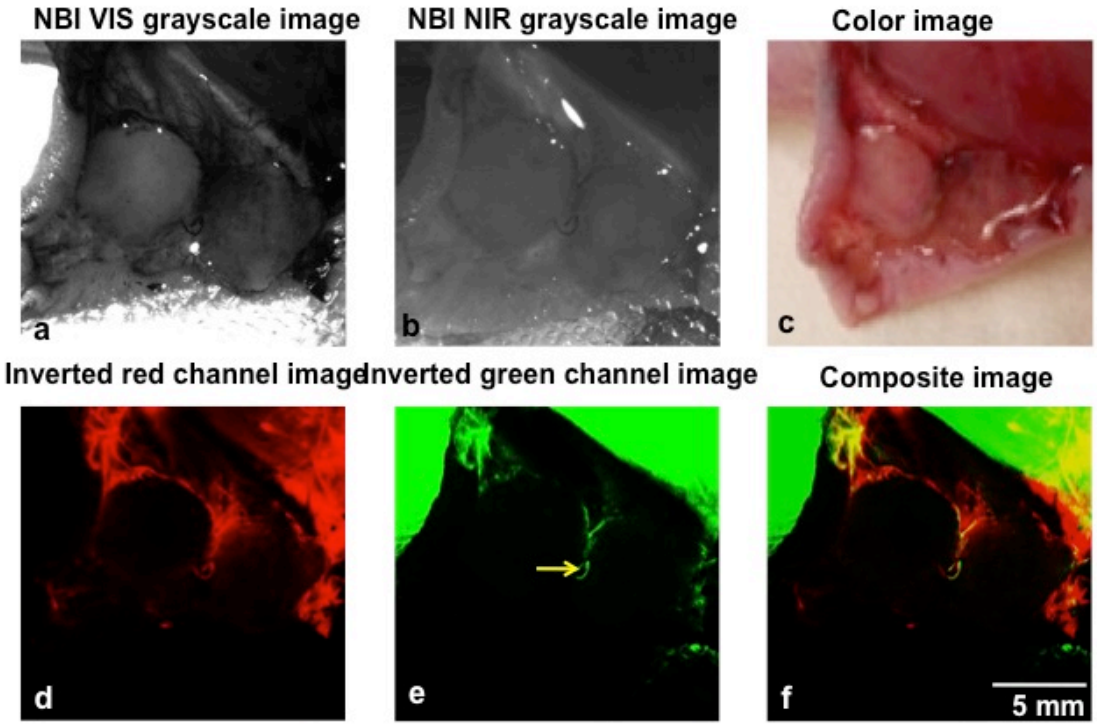

Figure 6.3. (a) Narrow band grayscale VIS image, (b) Narrow band grayscale NIR image, (c) Standard color image, (d) Narrow band VIS image assigned to red channel, (e) Narrow band NIR image assigned to green channel, and (f) Composite NBI image. The yellow arrow indicates GNRs.

6.3.3 *In vivo* NIR NBI imaging of folic acid conjugated gold nanorods topically administered on MCF-7 tumors

Figure 6.4 is a representative image of one of the three tumors that received topical delivery of folic acid conjugated GNRs imaged using NBI. Although the MCF-7 tumor line is known to express the folic Acid receptor, we did not observe nanorod labeling in the tumors after incubation for 30 minutes.

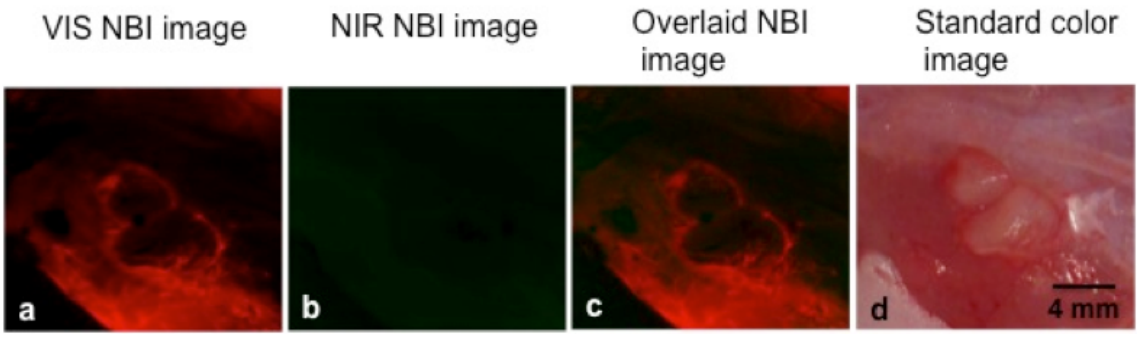

Figure 6.4. MCF-7 tumors topically administered with folic acid conjugated gold nanorods. (a) Narrow band VIS image assigned to red channel (b) Narrow band NIR image assigned to green channel (c) Composite NBI image (d) Corresponding standard color image.

6.3.4 *Ex vivo* imaging of pancreatic tumor margins

Figure 6.5 is a representative image of a tumor accumulated with RGD conjugated GNSs and imaged using bioluminescence and NBI. We demonstrated the ability of the NIR narrowband system to detect the low levels of gold nanoshells that accumulated within resection margins and the degree of overlap between bioluminescence imaging and NIR narrowband imaging.

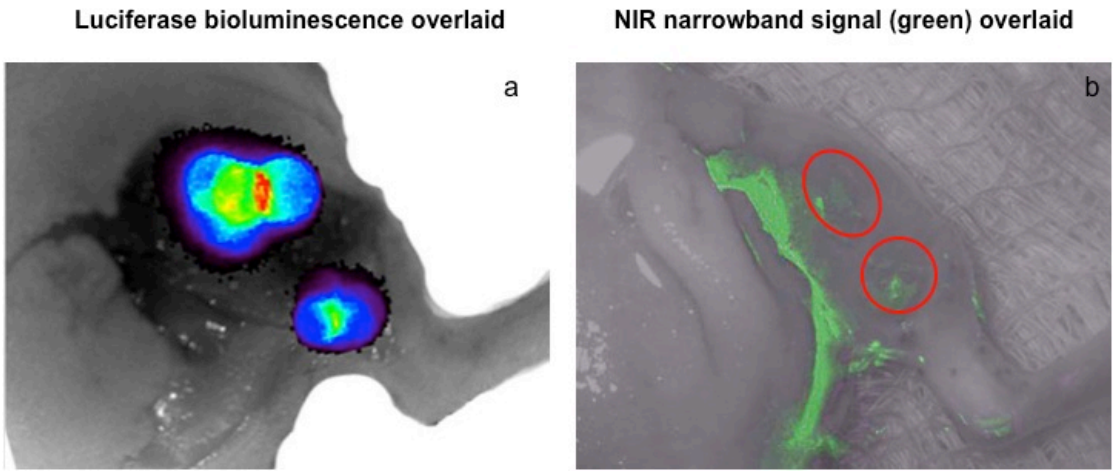

Figure 6.5: Sensing and imaging resection margins using conjugated gold nanoshells. (a) Bioluminescence imaging of resection margins in a mouse with a resected xenograft of luciferase transfected MiaPaca cells. (b) In the same mouse, injection of RGD conjugated gold nanoshells shows presence of the particles in the tumor bed post-surgery using NIR narrowband imaging (red circles).

6.3.5 *In vivo* image-guided therapy of pancreatic tumor margins

Figure 6.6 represents *in vivo* NBI of pancreatic tumor margin. We observed minimal signal from the conjugated gold nanoshells present in the margin. Following detection of conjugated GNSs, we performed image guided thermal ablation using the setup described in section 6.2.4. The laser ablation did not result in significant temperature increase to ablate the tumor cells and was confirmed using bioluminescence imaging.

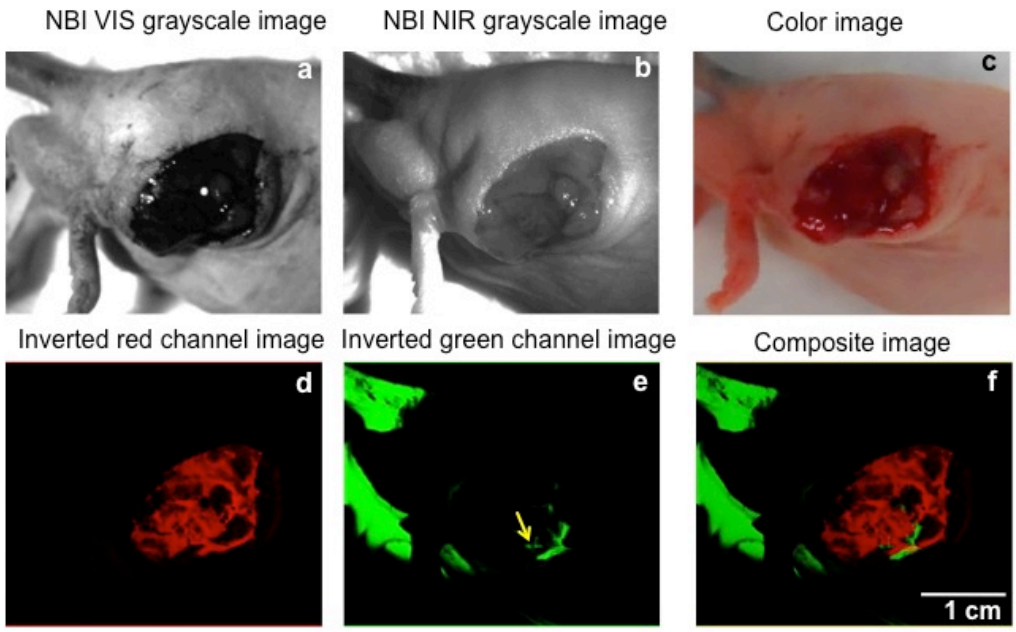

Figure 6.6. (a) Narrow band grayscale VIS image, (b) Narrow band grayscale NIR image, (c) Standard color image, (d) Narrow band VIS image assigned to red channel, (e) Narrow band NIR image assigned to green channel, and (f) Composite NBI image. The yellow arrow indicates RGD conjugated GNSs.

6.4 Discussion

In order to use the NIR NBI system for real-time tumor margin detection, we expected higher nanoparticle accumulations in the MCF-7 breast tumors. Although we could identify the GNRs present in some tumors, the nanorod accumulation concentration observed was very minimal. MCF-7 tumors are known to express high levels of folate receptor.[121] Therefore, we performed topically delivery of folic acid conjugated GNRs on the MCF-7 tumors. However, we did not observe any labeling following 30 minutes of incubation. Further analysis on the levels of folate receptor expression and specificity of the folic acid conjugated GNRs to these tumors are required.

The principal limitation in the breast tumor imaging study was the failure of the tumor/mouse model to yield rapidly growing breast tumors that would have provided a realistic proliferating vasculature for passively accumulated and topically delivered nanoparticles. We believe that *Fox 1*^{nu} nude mouse may not be an optimal model due to its very slow growth rate (~2- 3 months) resulting in a small tumor (mostly 3 x 3 x 1 mm). We have on-going work to identify a suitable breast tumor model and establish minimal residual disease for the same. The NBI system, however, demonstrated that it is robust (the system was transported and re-assembled for each of the imaging sessions), sensitive, and consistent. We anticipate that coupling the NIR NBI system with a successful *in vivo* model will provide pre-clinical, efficacy data that will justify its use in clinical settings.

The NBI images showing pancreatic tumor margin contained very few conjugated gold nanoshells (Figure 6.5 and 6.6). Spurious signal was noted at the skin fold along the tumor margin that could be due to effects of shadowing and index mismatch. However, good correspondence between bioluminescence and narrow-band imaging suggest that low levels of residual tumor are readily detectable using this technique.

Image guided thermal ablation performed in the pancreatic tumor margins did not produce significant heating to ablate the tumor cells. This was mainly due to inappropriate laser power settings and laser probe positioning. In order to conduct effective thermal therapy in the future, we intend to perform and test laser ablation in *ex*

vivo models and determine the optimum settings required to ablate the cancer cells without disturbing any normal tissue.

Chapter 7

Conclusion and future directions

7.1 Summary

There is a clear need for technology which will increase the percentage of patients achieving a clear margin with surgery. Therefore, any technology that could help a surgeon visualize the tumor at the margin intraoperatively would aid in achieving clear margins. This dissertation presents a novel imaging technique called near-infrared narrow-band imaging combined with gold nanoparticles as contrast agents to image tumor and its margins intraoperatively.

In the second chapter, we present the prototype NIR NBI system and demonstrate that the system can effectively highlight GNSs systemically delivered to tumors. We illuminated the target using broadband light and collected narrow band of images in the

VIS and NIR to highlight absorption of hemoglobin and GNS in colon tumor xenografts. We quantitatively identified the narrow wavelength bands for imaging that provides enhanced visualization of both hemoglobin and GNSs in tumors. The preliminary results obtained from *in vitro* and *ex vivo* imaging were promising and also suggested that NIR NBI is a feasible technique to identify positive margins during surgical resection of tumors. The identification of tumor regions is a first step to image-guided surgical removal of tumor margins or photo thermal therapy. The NBI technique could potentially provide a platform for integrated cancer imaging and therapy.

In Chapter 3, we discuss our efforts towards optimizing the prototype NIR NBI system to make it compact, portable as well as achieve real-time imaging capabilities. A filter wheel containing band pass filters was replaced with the LCTF to acquire two images; one in the visible and other in the near infrared portions of the spectrum to image the blood vessels and gold nanoparticles, respectively. The real-time imaging capabilities were achieved by having an AC motor control the filter wheel rotation and timed to trigger an optical interrupt to enable imaging at the filters position. The original quartz-halogen illumination system was replaced with visible and near infrared LED's which lowered the power requirements and increased the discrimination in simultaneously illuminating blood vessels and nanoparticles. We developed a graphical user interface to display the images and provide controls to dynamically adjust the image features such as brightness and contrast of each channel. The depth of imaging sensitivity was measured using physiologically relevant nanoparticle concentrations embedded at various depths

within a tissue-mimicking phantom. We did not observe loss of contrast until the nanoparticle concentration reached ~1.72 X 10^{11} particles/mL and a depth of approximately 2 mm, suggesting tumor visualization to that depth.

Chapter 4 investigates the effects of particle type, size and dosing on tumor targeting and accumulation for effective imaging and therapy. The results from NAA show that smaller particles have enhanced accumulation in tumors compared to larger nanoparticles. In addition, NAA data demonstrated that multiple nanoparticle dosing caused higher particle accumulation in tumors compared to a single dose. Histopathological analysis of the tissues confirmed no acute toxicity as an effect of multiple dosing. However, multiple dosing in mice did not contribute to increased NBI image contrast, which is considered a key to performing image-guided margin resection. In addition, we continued to observe heterogeneity in nanoparticle accumulation in tumors with multiple dosing that could affect effective photo-thermal tumor therapy.

In chapter 5, we utilized topically delivery approach to label the non-melanoma skin tumors using anti-EGFR antibody conjugated GNRs and imaged using NIR NBI. NBI demonstrated that the conjugated GNRs were effective probes for EGFR expression in squamous cell carcinomas. Using near-infrared NBI and two-photon microscopy, we demonstrated that anti-EGFR GNRs specifically bound to EGFRs over-expressed in A431 tumors and improved optical visualization of SCC tumors. The C225-GNRs attached to the over-expressed EGF receptors providing an enhanced intensity of up to

2.5 fold. Our data suggests that the combined use of targeted GNRs and near-infrared NBI may potentially aid in tumor margin assessment based on EGFR-expression levels serving as a valuable diagnostic tool during surgical resection of SCC tumors.

Finally, in chapter 6 we demonstrated the feasibility of using the real-time NBI system to image breast and pancreatic tumor margins intraoperatively. We also demonstrated feasibility of performing image-guided therapy of pancreatic tumor margins. In order to clinically translate the system to potentially perform NBI during surgery in humans, we need to execute further *in vivo* studies with a larger animal model, optimized laser parameters and suitable contrast agents.

7.2 Future Work

Our second-generation real-time narrow-band imaging system currently acquires and processes images at 6 fps. The existing system has proved the feasibility of performing intraoperative imaging of tumor and its margins. However, for clinical purposes, a faster image acquisition and processing is desirable. The rate-limiting step in the current system is the image processing that involves overlaying VIS and NIR grayscale images to obtain and display composite images. Therefore, integrating a graphics video card in the system could potentially increase the process. It will enable faster image processing/display and achieve imaging rates near the standard 30 fps (video-rate). Integrating a graphics video

card will potentially enable imaging 12 bit images eliminating the necessity to bin and therefore improve image resolution.

Additionally, our current real-time system collects two narrow-band images (NIR and VIS) sequentially. Motion artifacts due to the mouse's rapid cardiac and respiratory activity make this approach problematic. To completely eliminate these motion artifacts, the two frames need to be collected simultaneously. This could be accomplished by implementing a lens array system, which will acquire multiple narrow band images simultaneously through multiple independent imaging channels. Specifically, we will design and construct a multiaperture camera, based on a single CCD, using 2 (or more, as required) individual lenses, forming 2 separate sub images on a single CCD frame. In front of the 2 lenses we will mount a plate that will hold multiple individual optical elements such as band pass filters that alter the optical information in a single sub image. We believe that this approach will constitute an effective real-time imaging system, especially in conditions where motion artifacts are an issue.

We studied the effect of multiple dosing on nanoparticle accumulation in tumors for GNRs and GNSs. It will be interesting to study multiple dosing for different particle sizes for the same particle type (e.g. GNRs of different aspect ratios or GNSs of different diameters) for a particular tumor model and study their effect on tumor accumulation patterns and biodistribution. In addition, it will be interesting to study the effect of multiple dosing for different dilutions of a given nanoparticle type and size. Although we

have shown the effect of multiple dosing using passive targeting of pegylated GNPs in chapter 3, it will be interesting to see the effect when the particles are actively targeted (antibody conjugated to target specific receptor).

We demonstrated NBI of squamous cell carcinoma mouse tumors that received topical delivery of conjugated GNRs. The incubations times used in the study (30 minutes) were based on the optimum and standard time considered for particles to be taken up by cells. However, in order to use this delivery approach combined with intraoperative imaging during Mohs surgery, a shorter labeling time would be desirable. Therefore, we will perform *ex vivo* studies on mouse tumors and human tumor sections to determine an optimum and shorter incubation time that provides good tumor image contrast with respect to surrounding tissue for intraoperative NBI. We will use the optimum time determined through *ex vivo* studies to evaluate NBI of topically delivered conjugated GNPs in human skin tissues. We will obtain the human skin tissues from a tissue bank to conduct this study and demonstrate the capability of NBI system to image human tumors.

We tested the second-generation NBI system to perform *in vivo* tumor and tumor margin imaging in breast and pancreatic tumor models. We also attempted to perform image-guided thermal therapy. As a follow up to thermal therapy after optimizing the laser parameters, we will perform histology of the treated tumor samples to confirm ablation. Once the combined imaging and therapy is successful, we will perform

longitudinal tumor volume studies. We will perform longitudinal tumor volume studies to evaluate treatment outcome following image-guided therapy. The animal groups will be similar to section 6.2.3 (*in vivo* imaging animal group). Following photothermal therapy, animals in the sham-treatment and laser-treatment groups will undergo bioluminescence imaging. Subsequently, all animals will undergo bioluminescence-imaging twice weekly to check for local recurrence as well as metastasis. We will euthanize the mice after 4 weeks to measure tumor volume. We will perform statistical analysis to determine significant difference among the groups. If successful, we will perform a preclinical longitudinal tumor volume study to evaluate treatment outcomes following image-guided therapy with GNPs.

Bibliography

1. T. Sohn, C. Yeo, J. Cameron, L. Koniaris, S. Kaushal, R. Abrams, P. Sauter, J. Coleman, R. Hruban and K. Lillemoe, "Resected adenocarcinoma of the pancreas-616 patients: results, outcomes, and prognostic indicators," Journal of Gastrointestinal Surgery 4(6), 567-579 (2000)

2. J. Neoptolemos, D. Stocken, J. Dunn, J. Almond, H. Beger, P. Pederzoli, C. Bassi, C. Dervenis, L. Fernandez-Cruz and F. Lacaine, "Influence of resection margins on survival for patients with pancreatic cancer treated by adjuvant chemoradiation and/or chemotherapy in the ESPAC-1 randomized controlled trial," Annals of Surgery 234(6), 758 (2001)

3. K. Millikan, D. Deziel, J. Silverstein, T. Kanjo, J. Christein, A. Doolas and R. Prinz, "Prognostic factors associated with resectable adenocarcinoma of the head of the pancreas," The American surgeon 65(7), 618 (1999)

4. G. Benassai, M. Mastrorilli, G. Quarto, A. Cappiello, U. Giani and G. Mosella, "Survival after pancreaticoduodenectomy for ductal adenocarcinoma of the head of the pancreas," Chirurgia italiana 52(3), 263

5. K. Kuhlmann, S. de Castro, J. Wesseling, F. ten Kate, G. Offerhaus, O. Busch, T. van Gulik, H. Obertop and D. Gouma, "Surgical treatment of pancreatic adenocarcinoma actual survival and prognostic factors in 343 patients," European Journal of Cancer 40(4), 549-558 (2004)

6. F. Gall, H. Kessler and P. Hermanek, "Surgical treatment of ductal pancreatic carcinoma," European Journal of Surgical Oncology 17(2), 173 (1991)

7. M. Trede, G. Schwall and H. Saeger, "Survival after pancreatoduodenectomy. 118 consecutive resections without an operative mortality," Annals of Surgery 211(4), 447 (1990)

8. C. Willett, K. Lewandrowski, A. Warshaw, J. Efird and C. Compton, "Resection margins in carcinoma of the head of the pancreas. Implications for radiation therapy," Annals of Surgery 217(2), 144 (1993)

9. S. Nitecki, M. Sarr, T. Colby and J. Van Heerden, "Long-term survival after resection for ductal adenocarcinoma of the pancreas. Is it really improving?," Annals of Surgery 221(1), 59 (1995)

10. J. Birkmeyer, T. Stukel, A. Siewers, P. Goodney, D. Wennberg and F. Lucas, "Surgeon volume and operative mortality in the United States," The New England journal of medicine 349(22), 2117 (2003)

11. D. P. O'Neal, L. R. Hirsch, N. J. Halas, J. D. Payne and J. L. West, "Photo-thermal tumor ablation in mice using near infrared-absorbing nanoparticles," Cancer Letters 209(2), 171-176 (2004)

12. A. Barros, M. Pinotti, M. D. Ricci, A. C. Nisida and J. A. Pinotti, "Immediate effects of intraoperative evaluation of surgical margins over the treatment of early infiltrating breast carcinoma," Tumori 89(1), 42-45 (2003)

13. T. L. Huston, R. Pigalarga, M. P. Osborne and E. Tousimis, "The influence of additional surgical margins on the total specimen volume excised and the reoperative rate after breast-conserving surgery," Am J Surg 192(4), 509-512 (2006)

14. V. S. Klimberg, J. Kepple, G. Shafirstein, L. Adkins, R. Henry-Tillman, E. Youssef, J. Brito, L. Talley and S. Korourian, "eRFA: excision followed by RFA-a new technique to improve local control in breast cancer," Ann Surg Oncol 13(11), 1422-1433 (2006)

15. E. R. Fisher, S. Anderson, E. Tan-Chiu, B. Fisher, L. Eaton and N. Wolmark, "Fifteen-year prognostic discriminants for invasive breast carcinoma: National Surgical Adjuvant Breast and Bowel Project Protocol-06," Cancer 91(8 Suppl), 1679-1687 (2001)

16. U. Veronesi, A. Luini, M. Del Vecchio, M. Greco, V. Galimberti, M. Merson, F. Rilke, V. Sacchini, R. Saccozzi, T. Savio and et al., "Radiotherapy after breast-preserving surgery in women with localized cancer of the breast," N Engl J Med 328(22), 1587-1591 (1993)

17. R. M. Clark, T. Whelan, M. Levine, R. Roberts, A. Willan, P. McCulloch, M. Lipa, R. H. Wilkinson and L. J. Mahoney, "Randomized clinical trial of breast irradiation following lumpectomy and axillary dissection for node-negative breast cancer: an update. Ontario Clinical Oncology Group," J Natl Cancer Inst 88(22), 1659-1664 (1996)

18. M. Rajadhyaksha, G. Menaker, T. Flotte, P. J. Dwyer and S. Gonzalez, "Confocal examination of nonmelanoma cancers in thick skin excisions to potentially guide mohs micrographic surgery without frozen histopathology," J Invest Dermatol 117(5), 1137-1143 (2001)

19. S. E. Skrabalak, L. Au, X. Lu, X. Li and Y. Xia, "Gold nanocages for cancer detection and treatment," Nanomed 2(5), 657-668 (2007)

20. T. S. Troutman, J. K. Barton and M. Romanowski, "Optical coherence tomography with plasmon resonant nanorods of gold," Opt Lett 32(11), 1438-1440 (2007)

21. C. Loo, A. Lin, L. Hirsch, M. H. Lee, J. Barton, N. Halas, J. West and R. Drezek, "Nanoshell-enabled photonics-based imaging and therapy of cancer," Technol Cancer Res Treat 3(1), 33-40 (2004)

22. J. A. Copland, M. Eghtedari, V. L. Popov, N. Kotov, N. Mamedova, M. Motamedi and A. A. Oraevsky, "Bioconjugated gold nanoparticles as a molecular based contrast agent: implications for imaging of deep tumors using optoacoustic tomography," Mol Imaging Biol 6(5), 341-349 (2004)

23. X. Yang, S. E. Skrabalak, Z. Y. Li, Y. Xia and L. V. Wang, "Photoacoustic tomography of a rat cerebral cortex in vivo with au nanocages as an optical contrast agent," Nano Lett 7(12), 3798-3802 (2007)

24. M. C. Pierce, D. J. Javier and R. Richards-Kortum, "Optical contrast agents and imaging systems for detection and diagnosis of cancer," Int J Cancer 123(9), 1979-1990 (2008)

25. S. A. Toms, W. C. Lin, R. J. Weil, M. D. Johnson, E. D. Jansen and A. Mahadevan-Jansen, "Intraoperative optical spectroscopy identifies infiltrating glioma margins with high sensitivity," Neurosurgery 57(4 Suppl), 382-391; discussion 382-391 (2005)

26. S. C. Gebhart, W. C. Lin and A. Mahadevan-Jansen, "In vitro determination of normal and neoplastic human brain tissue optical properties using inverse adding-doubling," Phys Med Biol 51(8), 2011-2027 (2006)

27. W. C. Lin, S. A. Toms, M. Johnson, E. D. Jansen and A. Mahadevan-Jansen, "In vivo brain tumor demarcation using optical spectroscopy," Photochem Photobiol 73(4), 396-402 (2001)

28. R. Trehin, J. L. Figueiredo, M. J. Pittet, R. Weissleder, L. Josephson and U. Mahmood, "Fluorescent nanoparticle uptake for brain tumor visualization," Neoplasia 8(4), 302-311 (2006)

29. V. Humblet, R. Lapidus, L. R. Williams, T. Tsukamoto, C. Rojas, P. Majer, B. Hin, S. Ohnishi, A. M. De Grand, A. Zaheer, J. T. Renze, A. Nakayama, B. S. Slusher and J. V. Frangioni, "High-affinity near-infrared fluorescent small-molecule contrast agents for in vivo imaging of prostate-specific membrane antigen," Mol Imaging 4(4), 448-462 (2005)

30. M. N. Rhyner, A. M. Smith, X. Gao, H. Mao, L. Yang and S. Nie, "Quantum dots and multifunctional nanoparticles: new contrast agents for tumor imaging," Nanomed 1(2), 209-217 (2006)

31. M. Veiseh, P. Gabikian, S. B. Bahrami, O. Veiseh, M. Zhang, R. C. Hackman, A. C. Ravanpay, M. R. Stroud, Y. Kusuma, S. J. Hansen, D. Kwok, N. M. Munoz, R. W. Sze, W. M. Grady, N. M. Greenberg, R. G. Ellenbogen and J. M. Olson, "Tumor paint: a chlorotoxin:Cy5.5 bioconjugate for intraoperative visualization of cancer foci," Cancer Res 67(14), 6882-6888 (2007)

32. K. Gono, T. Obi, M. Yamaguchi, N. Ohyama, H. Machida, Y. Sano, S. Yoshida, Y. Hamamoto and T. Endo, "Appearance of enhanced tissue features in narrow-band endoscopic imaging," Journal of Biomedical Optics 9(3), 568-577 (2004)

33. T. Yoshida, H. Inoue, S. Usui, H. Satodate, N. Fukami and S. Kudo, "Narrow-band imaging system with magnifying endoscopy for superficial esophageal lesions," Gastrointestinal Endoscopy 59(2), 288-295 (2004)

34. R. T. Bryan, L. J. Billingham and D. M. Wallace, "Narrow-band imaging flexible cystoscopy in the detection of recurrent urothelial cancer of the bladder," BJU Int 101(6), 702-705; discussion 705-706 (2008)

35. M. Farrugia, M. S. Nair and K. V. Kotronis, "Narrow band imaging in endometriosis," J Minim Invasive Gynecol 14(4), 393-394 (2007)

36. Y. Hamamoto, T. Endo, K. Nosho, Y. Arimura, M. Sato and K. Imai, "Usefulness of narrow-band imaging endoscopy for diagnosis of Barrett's esophagus," J Gastroenterol 39(1), 14-20 (2004)

37. C. Piazza, O. Dessouky, G. Peretti, D. Cocco, L. De Benedetto and P. Nicolai, "Narrow-band imaging: a new tool for evaluation of head and neck squamous cell

carcinomas. Review of the literature," Acta Otorhinolaryngol Ital 28(2), 49-54 (2008)

38. S. J. Oldenburg, R. D. Averitt, S. L. Westcott and N. J. Halas, "Nanoengineering of optical resonances," Chemical Physics Letters 288(2-4), 243-247 (1998)

39. R. D. Averitt, D. Sarkar and N. J. Halas, "Plasmon Resonance Shifts of Au-Coated Au~ 2S Nanoshells: Insight into Multicomponent Nanoparticle Growth," Physical Review Letters 78(22), 4217-4220 (1997)

40. S. J. Oldenburg, G. D. Hale, J. B. Jackson and N. J. Halas, "Light scattering from dipole and quadrupole nanoshell antennas," Applied Physics Letters 75(1063 (1999)

41. E. Prodan and P. Nordlander, "Structural tunability of the plasmon resonances in metallic nanoshells," Nano Letters 3(4), 543-547 (2003)

42. C. Loo, A. Lowery, N. Halas, J. West and R. Drezek, "Immunotargeted nanoshells for integrated cancer imaging and therapy," Nano Letters 5(4), 709-711 (2005)

43. K. Sokolov, M. Follen, J. Aaron, I. Pavlova, A. Malpica, R. Lotan and R. Richards-Kortum, "Real-Time Vital Optical Imaging of Precancer Using Anti-Epidermal Growth Factor Receptor Antibodies Conjugated to Gold Nanoparticles 1," pp. 1999-2004, AACR (2003).

44. C. Loo, L. Hirsch, M. H. Lee, E. Chang, J. West, N. Halas and R. Drezek, "Gold nanoshell bioconjugates for molecular imaging in living cells," Optics Letters 30(9), 1012-1014 (2005)

45. J. Yguerabide and E. E. Yguerabide, "Resonance light scattering particles as ultrasensitive labels for detection of analytes in a wide range of applications," Journal of Cellular Biochemistry 84(s 37), 71-81 (2001)

46. J. Park, A. Estrada, K. Sharp, K. Sang, J. A. Schwartz, D. K. Smith, C. Coleman, J. D. Payne, B. A. Korgel, A. K. Dunn and J. W. Tunnell, "Two-photon-induced photoluminescence imaging of tumors using near-infrared excited gold nanoshells," Opt Express 16(3), 1590-1599 (2008)

47. H. Maeda, J. Fang, T. Inutsuka and Y. Kitamoto, "Vascular permeability enhancement in solid tumor: various factors, mechanisms involved and its implications," International Immunopharmacology 3(3), 319-328 (2003)

48. A. R. Lowery, A. M. Gobin, E. S. Day, N. J. Halas and J. L. West, "Immunonanoshells for targeted photothermal ablation of tumor cells," Int J Nanomedicine 1(2), 149-154 (2006)

49. G. von Maltzahn, J. Park, A. Agrawal, N. Bandaru, S. Das, M. Sailor and S. Bhatia, "Computationally Guided Photothermal Tumor Therapy Using Long-Circulating Gold Nanorod Antennas," Cancer Research 69(9), 3892 (2009)

50. L. Tong, Y. Zhao, T. B. Huff, M. N. Hansen, A. Wei and J. X. Cheng, "Gold Nanorods Mediate Tumor Cell Death by Compromising Membrane Integrity," Adv Mater Deerfield 19(3136-3141 (2007)

51. T. B. Huff, L. Tong, Y. Zhao, M. N. Hansen, J. X. Cheng and A. Wei, "Hyperthermic effects of gold nanorods on tumor cells," Nanomedicine (Lond) 2(1), 125-132 (2007)

52. T. Hauck, T. Jennings, T. Yatsenko, J. Kumaradas, W. Chan and K. Foundation, "Enhancing the toxicity of cancer chemotherapeutics with gold nanorod hyperthermia," Adv Mater 20(2832ñ2838 (2008)

53. X. Huang, I. H. El-Sayed, W. Qian and M. A. El-Sayed, "Cancer cell imaging and photothermal therapy in the near-infrared region by using gold nanorods," J Am Chem Soc 128(6), 2115-2120 (2006)

54. Y. F. Huang, K. Sefah, S. Bamrungsap, H. T. Chang and W. Tan, "Selective photothermal therapy for mixed cancer cells using aptamer-conjugated nanorods," Langmuir 24(20), 11860-11865 (2008)

55. L. R. Hirsch, R. J. Stafford, J. A. Bankson, S. R. Sershen, B. Rivera, R. E. Price, J. D. Hazle, N. J. Halas and J. L. West, "Nanoshell-mediated near-infrared thermal therapy of tumors under magnetic resonance guidance," Proceedings of the National Academy of Sciences 100(23), 13549-13554 (2003)

56. E. B. Dickerson, E. C. Dreaden, X. Huang, I. H. El-Sayed, H. Chu, S. Pushpanketh, J. F. McDonald and M. A. El-Sayed, "Gold nanorod assisted near-infrared plasmonic photothermal therapy (PPTT) of squamous cell carcinoma in mice," Cancer Lett 269(1), 57-66 (2008)

57. G. Goodrich, L. Bao, K. Gill-Sharp, K. Sang, J. Wang and J. Payne, "Photothermal therapy in a murine colon cancer model using near-infrared absorbing gold nanorods," Journal of Biomedical Optics 15(018001

58. A. Lin, L. Hirsch, M. H. Lee, J. Barton, N. Halas, J. West and R. Drezek, "Nanoshell-Enabled Photonics-Based Imaging and Therapy of Cancer," Technology in Cancer Research & Treatment 3(1), (2004)

59. C. Loo, A. Lowery, N. Halas, J. West and R. Drezek, "Immunotargeted nanoshells for integrated cancer imaging and therapy," Nano Lett 5(4), 709–711 (2005)

60. A. M. Gobin, M. H. Lee, N. J. Halas, W. D. James, R. A. Drezek and J. L. West, "Near-infrared resonant nanoshells for combined optical imaging and photothermal cancer therapy," Nano Letters 7(7), 1929–1934 (2007)

61. A. Agrawal, S. Huang, A. W. H. Lin, M. H. Lee, J. K. Barton, R. A. Drezek and T. J. Pfefer, "Quantitative evaluation of optical coherence tomography signal enhancement with gold nanoshells," Journal of Biomedical Optics 11(041121 (2006)

62. Y. Wang, X. Xie, X. Wang, G. Ku, K. L. Gill, D. P. O'Neal, G. Stoica and L. V. Wang, "Photoacoustic Tomography of a Nanoshell Contrast Agent in the in Vivo Rat Brain," times 12(13

63. I. H. El-Sayed, X. Huang and M. A. El-Sayed, "Selective laser photo-thermal therapy of epithelial carcinoma using anti-EGFR antibody conjugated gold nanoparticles," Cancer Letters 239(1), 129-135 (2006)

64. I. H. El-Sayed, X. Huang and M. A. El-Sayed, "Surface plasmon resonance scattering and absorption of anti-EGFR antibody conjugated gold nanoparticles in cancer diagnostics: applications in oral cancer," Nano Lett 5(5), 829–834 (2005)

65. L. Bickford, J. Sun, K. Fu, N. Lewinski, V. Nammalvar, J. Chang and R. Drezek, "Enhanced multi-spectral imaging of live breast cancer cells using immunotargeted gold nanoshells and two-photon excitation microscopy," Nanotechnology 19(315102), 315102 (2008)

66. H. Machida, Y. Sano, Y. Hamamoto, M. Muto, T. Kozu, H. Tajiri and S. Yoshida, "Narrow-band imaging in the diagnosis of colorectal mucosal lesions: a pilot study," Endoscopy 36(12), 1094-1098 (2004)

67. W. D. James, L. R. Hirsch, J. L. West, P. D. O'Neal and J. D. Payne, "Application of INAA to the build-up and clearance of gold nanoshells in clinical studies in mice," Journal of Radioanalytical and Nuclear Chemistry 271(2), 455-459 (2007)

68. R. T. Zaman, P. Diagaradjane, J. C. Wang, J. Schwartz, N. Rajaram, K. L. Gill-Sharp, S. H. Cho, H. G. Rylander III, J. D. Payne, S. Krishnan and J. W. Tunnell, "*In Vivo* Detection of Gold Nanoshells in Tumors Using Diffuse Optical Spectroscopy," IEEE Journal of Selected Topics in Quantum Electronics 13(6), 1715-1720 (2007)

69. A.K.Jain, *Fundamentals of Digital Image Processing*, Prentice-Hall, NJ (1988).

70. M. M. Haglund, M. S. Berger and D. W. Hochman, "Enhanced Optical Imaging of Human Gliomas and Tumor Margins," Neurosurgery 38(2), 308 (1996)

71. A. J. Welch and M. J. C. van Gemert, Optical-thermal Response of Laser-irradiated Tissue, Plenum Pub Corp (1995).

72. M. L. Li, J. A. Schwartz, J. Wang, G. Stoica and L. V. Wang, "*In vivo* imaging of nanoshell extravasation from solid tumor vasculature by photoacoustic microscopy," in Proc of SPIE, p. 64370B, SPIE (2007).

73. P. Diagaradjane, A. Shetty, J. C. Wang, A. M. Elliott, J. Schwartz, S. Shentu, H. C. Park, A. Deorukhkar, R. J. Stafford and S. H. Cho, "Modulation of *in Vivo* Tumor Radiation Response via Gold Nanoshell-Mediated Vascular-Focused Hyperthermia: Characterizing an Integrated Antihypoxic and Localized Vascular Disrupting Targeting Strategy," Nano Letters (2008)

74. C. H. Choi, C. A. Alabi, P. Webster and M. E. Davis, "Mechanism of active targeting in solid tumors with transferrin-containing gold nanoparticles," Proc Natl Acad Sci U S A 107(3), 1235-1240

75. K. J. Williams, B. A. Telfer, I. J. Stratford and S. R. Wedge, "ZD1839 ('Iressa'), a specific oral epidermal growth factor receptor-tyrosine kinase inhibitor, potentiates radiotherapy in a human colorectal cancer xenograft model," British Journal of Cancer 86(7), 1157-1161 (2002)

76. T. Kato, K. Sato, H. Kakinuma and Y. Matsuda, "Enhanced suppression of tumor growth by combination of angiogenesis inhibitor O-(chloroacetyl-carbamoyl)fumagillol (TNP-470) and cytotoxic agents in mice," Cancer Research 54(19), 5143-5147 (1994)

77. D. Santini, B. Vincenzi, A. La Cesa, V. Virzi, F. Navajas, V. Malafarina, G. Dicuonzo, R. Cassandro, V. Esposito, V. Montesarchio, A. M. Groeger and G. Tonini, "A new dose-intense epoetin alfa regimen effective in anemic cancer

patients receiving chemotherapy: an open-label, non randomized, pilot study," Anticancer Research 25(1B), 669-674 (2005)

78. D. E. Dolmans, A. Kadambi, J. S. Hill, K. R. Flores, J. N. Gerber, J. P. Walker, I. H. Borel Rinkes, R. K. Jain and D. Fukumura, "Targeting tumor vasculature and cancer cells in orthotopic breast tumor by fractionated photosensitizer dosing photodynamic therapy," Cancer Research 62(15), 4289-4294 (2002)

79. W. H. De Jong, W. I. Hagens, P. Krystek, M. C. Burger, A. J. Sips and R. E. Geertsma, "Particle size-dependent organ distribution of gold nanoparticles after intravenous administration," Biomaterials 29(12), 1912-1919 (2008)

80. G. S. Terentyuk, G. N. Maslyakova, L. V. Suleymanova, B. N. Khlebtsov, B. Y. Kogan, G. G. Akchurin, A. V. Shantrocha, I. L. Maksimova, N. G. Khlebtsov and V. V. Tuchin, "Circulation and distribution of gold nanoparticles and induced alterations of tissue morphology at intravenous particle delivery," J Biophotonics 2(5), 292-302 (2009)

81. M. P. Melancon, W. Lu, Z. Yang, R. Zhang, Z. Cheng, A. M. Elliot, J. Stafford, T. Olson, J. Z. Zhang and C. Li, "In vitro and in vivo targeting of hollow gold nanoshells directed at epidermal growth factor receptor for photothermal ablation therapy," Molecular Cancer Therapeutics 7(6), 1730 (2008)

82. J. Wang, J. D. Byrne, M. E. Napier and J. M. DeSimone, "More effective nanomedicines through particle design," Small 7(14), 1919-1931

83. T. Nomura, N. Koreeda, F. Yamashita, Y. Takakura and M. Hashida, "Effect of particle size and charge on the disposition of lipid carriers after intratumoral injection into tissue-isolated tumors," Pharm Res 15(1), 128-132 (1998)

84. S. Hu-Lieskovan, J. D. Heidel, D. W. Bartlett, M. E. Davis and T. J. Triche, "Sequence-specific knockdown of EWS-FLI1 by targeted, nonviral delivery of small interfering RNA inhibits tumor growth in a murine model of metastatic Ewing's sarcoma," Cancer Research 65(19), 8984-8992 (2005)

85. M. E. Davis, Z. G. Chen and D. M. Shin, "Nanoparticle therapeutics: an emerging treatment modality for cancer," Nat Rev Drug Discov 7(9), 771-782 (2008)

86. S. D. Perrault, C. Walkey, T. Jennings, H. C. Fischer and W. C. Chan, "Mediating tumor targeting efficiency of nanoparticles through design," Nano Letters 9(5), 1909-1915 (2009)

87. N. R. Jana, L. Gearheart and C. J. Murphy, "Wet chemical synthesis of high aspect ratio cylindrical gold nanorods," The Journal of Physical Chemistry B 105(19), 4065-4067 %@ 1520-6106 (2001)

88. G. Goodrich, L. Bao, K. Gill-Sharp, K. Sang, J. Wang and J. Payne, "Photothermal therapy in a murine colon cancer model using near-infrared absorbing gold nanorods," Journal of Biomedical Optics 15(018001 (2010)

89. D. W. Bartlett and M. E. Davis, "Impact of tumor-specific targeting and dosing schedule on tumor growth inhibition after intravenous administration of siRNA-containing nanoparticles," Biotechnol Bioeng 99(4), 975-985 (2008)

90. J. Park, A. Estrada, J. A. Schwartz, P. Diagaradjane, S. Krishnan, A. K. Dunn and J. W. Tunnell, "Intra-organ Biodistribution of Gold Nanoparticles Using Intrinsic Two-photon Induced Photoluminescence," Lasers in Surgery and Medicine 42(7), 630-639 (2010)

91. P. Puvanakrishnan, P. Diagaradjane, S. Kazmi, A. K. Dunn, S. Krishnan and T. J.W., "Narrow band imaging of squamous cell carcinoma tumors using topically delivered anti-EGFR antibody conjugated gold nanorods," Lasers Surg Med (In review)((2011)

92. R. K. Jain, "Transport of molecules, particles, and cells in solid tumors," Annu Rev Biomed Eng 1(241-263 (1999)

93. R. K. Jain and L. T. Baxter, "Mechanisms of heterogeneous distribution of monoclonal antibodies and other macromolecules in tumors: significance of elevated interstitial pressure," Cancer Research 48(24 Pt 1), 7022-7032 (1988)

94. Y. Boucher, L. T. Baxter and R. K. Jain, "Interstitial pressure gradients in tissue-isolated and subcutaneous tumors: implications for therapy," Cancer Research 50(15), 4478-4484 (1990)

95. H. S. Choi, W. Liu, P. Misra, E. Tanaka, J. P. Zimmer, B. Itty Ipe, M. G. Bawendi and J. V. Frangioni, "Renal clearance of quantum dots," Nat Biotechnol 25(10), 1165-1170 (2007)

96. S. K. Hobbs, W. L. Monsky, F. Yuan, W. G. Roberts, L. Griffith, V. P. Torchilin and R. K. Jain, "Regulation of transport pathways in tumor vessels: role of tumor type and microenvironment," Proc Natl Acad Sci U S A 95(8), 4607-4612 (1998)

97. A. Jemal, R. Siegel, E. Ward, Y. Hao, J. Xu and M. J. Thun, "Cancer Statistics, 2009," CA: A Cancer Journal for Clinicians 59(4), 225-249 (2009)

98. A. N. Yaroslavsky, V. Neel and R. R. Anderson, "Demarcation of nonmelanoma skin cancer margins in thick excisions using multispectral polarized light imaging," J Invest Dermatol 121(2), 259-266 (2003)

99. A. N. Yaroslavsky, J. Barbosa, V. Neel, C. DiMarzio and R. R. Anderson, "Combining multispectral polarized light imaging and confocal microscopy for localization of nonmelanoma skin cancer," J Biomed Opt 10(1), 14011 (2005)

100. Z. Tannous, A. Torres and S. Gonzalez, "In vivo real-time confocal reflectance microscopy: a noninvasive guide for Mohs micrographic surgery facilitated by aluminum chloride, an excellent contrast enhancer," Dermatol Surg 29(8), 839-846 (2003)

101. V. Q. Chung, P. J. Dwyer, K. S. Nehal, M. Rajadhyaksha, G. M. Menaker, C. Charles and S. B. Jiang, "Use of ex vivo confocal scanning laser microscopy during Mohs surgery for nonmelanoma skin cancers," Dermatol Surg 30(12 Pt 1), 1470-1478 (2004)

102. M. C. Pierce, J. Strasswimmer, B. H. Park, B. Cense and J. F. de Boer, "Advances in optical coherence tomography imaging for dermatology," J Invest Dermatol 123(3), 458-463 (2004)

103. J. Strasswimmer, M. C. Pierce, B. H. Park, V. Neel and J. F. de Boer, "Polarization-sensitive optical coherence tomography of invasive basal cell carcinoma," J Biomed Opt 9(2), 292-298 (2004)

104. L. Brancaleon, A. J. Durkin, J. H. Tu, G. Menaker, J. D. Fallon and N. Kollias, "In vivo fluorescence spectroscopy of nonmelanoma skin cancer," Photochem Photobiol 73(2), 178-183 (2001)

105. R. D. Averitt, S. L. Westcott and N. J. Halas, "Linear optical properties of gold nanoshells," Journal of the Optical Society of America B 16(10), 1824-1832 (1999)

106. C. Loo, A. Lowery, N. Halas, J. West and R. Drezek, "Immunotargeted nanoshells for integrated cancer imaging and therapy," Nano Lett 5(4), 709-711 (2005)

107. N. Nitin, K. J. Rosbach, A. El-Naggar, M. Williams, A. Gillenwater and R. R. Richards-Kortum, "Optical molecular imaging of epidermal growth factor receptor expression to improve detection of oral neoplasia," Neoplasia 11(6), 542-551 (2009)

108. L. R. Bickford, G. Agollah, R. Drezek and T. K. Yu, "Silica-gold nanoshells as potential intraoperative molecular probes for HER2-overexpression in ex vivo breast tissue using near-infrared reflectance confocal microscopy," Breast Cancer Res Treat 120(3), 547-555 (2010)

109. L. N. Klapper, M. H. Kirschbaum, M. Sela and Y. Yarden, "Biochemical and clinical implications of the ErbB/HER signaling network of growth factor receptors," Adv Cancer Res 77(25-79 (2000)

110. S. M. Huang and P. M. Harari, "Epidermal growth factor receptor inhibition in cancer therapy: biology, rationale and preliminary clinical results," Invest New Drugs 17(3), 259-269 (1999)

111. E. Maubec, P. Duvillard, V. Velasco, B. Crickx and M. F. Avril, "Immunohistochemical analysis of EGFR and HER-2 in patients with metastatic squamous cell carcinoma of the skin," Anticancer Res 25(2B), 1205-1210 (2005)

112. T. Shimizu, H. Izumi, A. Oga, H. Furumoto, T. Murakami, R. Ofuji, M. Muto and K. Sasaki, "Epidermal growth factor receptor overexpression and genetic aberrations in metastatic squamous-cell carcinoma of the skin," Dermatology 202(3), 203-206 (2001)

113. N. J. Durr, T. Larson, D. K. Smith, B. A. Korgel, K. Sokolov and A. Ben-Yakar, "Two-photon luminescence imaging of cancer cells using molecularly targeted gold nanorods," Nano Lett 7(4), 941-945 (2007)

114. M. P. Melancon, W. Lu, Z. Yang, R. Zhang, Z. Cheng, A. M. Elliot, J. Stafford, T. Olson, J. Z. Zhang and C. Li, "In vitro and in vivo targeting of hollow gold nanoshells directed at epidermal growth factor receptor for photothermal ablation therapy," Mol Cancer Ther 7(6), 1730-1739 (2008)

115. J. Park, A. Estrada, J. A. Schwartz, P. Diagaradjane, S. Krishnan, A. K. Dunn and J. W. Tunnell, "Intra-organ Biodistribution of Gold Nanoparticles Using Intrinsic Two-photon Induced Photoluminescence," Lasers Surg Med 42(7), 630-639

116. A. J. Haes, D. A. Stuart, S. Nie and R. P. Van Duyne, "Using solution-phase nanoparticles, surface-confined nanoparticle arrays and single nanoparticles as biological sensing platforms," J Fluoresc 14(4), 355-367 (2004)

117. J. Aaron, N. Nitin, K. Travis, S. Kumar, T. Collier, S. Y. Park, M. Jose-Yacaman, L. Coghlan, M. Follen, R. Richards-Kortum and K. Sokolov, "Plasmon resonance

coupling of metal nanoparticles for molecular imaging of carcinogenesis in vivo," J Biomed Opt 12(3), 034007 (2007)

118. R. K. Jain and L. T. Baxter, "Mechanisms of heterogeneous distribution of monoclonal antibodies and other macromolecules in tumors: significance of elevated interstitial pressure," Cancer Res 48(24 Pt 1), 7022-7032 (1988)

119. M. Mimeault, R. Brand, A. Sasson and S. Batra, "Recent advances on the molecular mechanisms involved in pancreatic cancer progression and therapies," Pancreas 31(4), 301 (2005)

120. A. Sultana, C. Smith, D. Cunningham, N. Starling, D. Tait, J. Neoptolemos and P. Ghaneh, "Systematic review, including meta-analyses, on the management of locally advanced pancreatic cancer using radiation/combined modality therapy," British Journal of Cancer 96(8), 1183 (2007)

121. J. Pan and S. S. Feng, "Targeting and imaging cancer cells by folate-decorated, quantum dots (QDs)- loaded nanoparticles of biodegradable polymers," Biomaterials 30(6), 1176-1183 (2009)

Vita

Priyaveena Puvanakrishnan was born in Chennai, India in 1982. In 2005, she graduated in first class with distinction from Anna University and received a Bachelor of Engineering degree in Electronics and Instrumentation. After working at a software firm for 2 years, she joined the graduate school at the University of Texas at Austin to work with Prof. James Tunnell in Biomedical Engineering. She received a Masters in Biomedical Engineering in 2009.

This dissertation was typed by the author.
Email: priyaveena@gmail.com